Binary neutron star populations in the Milky Way

Cecilia Sgalletta [1,2]★ Giuliano Iorio [2,3]★ Michela Mapelli [2,3,4]★ M. Celeste Artale [2,3,5]
Lumen Boco,[1] Debatri Chattopadhyay [6] Andrea Lapi,[1] Andrea Possenti,[7] Stefano Rinaldi [8,9] and
Mario Spera [1,10]

[1] *SISSA, Via Bonomea 365, I–34136 Trieste, Italy*
[2] *INFN–Padova, Via Marzolo 8, I–35131 Padova, Italy*
[3] *Dipartimento di Fisica e Astronomia Galileo Galilei, Università di Padova, Vicolo dell'Osservatorio 3, I–35122 Padova, Italy*
[4] *Universität Heidelberg, Zentrum für Astronomie, Institut für Theoretische Astrophysik, Albert-Ueberle-Str 2, D-69120 Heidelberg, Germany*
[5] *Departamento de Ciencias Fisicas, Universidad Andres Bello, Fernandez Concha 700, Las Condes, Santiago, Chile*
[6] *Gravity Exploration Institute, School of Physics and Astronomy, Cardiff University, Cardiff CF24 3AA, UK*
[7] *INAF–Osservatorio Astronomico di Cagliari, Via della Scienza 5, I-09047 Selargius, CA, Italy*
[8] *Dipartimento di Fisica 'E. Fermi', Università di Pisa, I-56127 Pisa, Italy*
[9] *INFN, Sezione di Pisa, I-56127 Pisa, Italy*
[10] *National Institute for Nuclear Physics – INFN, Sezione di Trieste, I-34127 Trieste, Italy*

ABSTRACT

Galactic binary neutron stars (BNSs) are a unique laboratory to probe the evolution of BNSs and their progenitors. Here, we use a new version of the population synthesis code SEVN to evolve the population of Galactic BNSs, by modelling the spin up and down of pulsars self-consistently. We analyse the merger rate $\mathcal{R}_{\mathrm{MW}}$, orbital period P_{orb}, eccentricity e, spin period P, and spin period derivative $\dot{P}$ of the BNS population. Values of the common envelope parameter $\alpha = 1-3$ and an accurate model of the Milky Way star formation history best reproduce the BNS merger rate in our Galaxy ($\mathcal{R}_{\mathrm{MW}} \approx 30\ \mathrm{Myr}^{-1}$). We apply radio-selection effects to our simulated BNSs and compare them to the observed population. Using a Dirichlet process Gaussian mixture method, we evaluate the four-dimensional likelihood in the (P_{orb}, e, P, $\dot{P}$) space, by comparing our radio-selected simulated pulsars against Galactic BNSs. Our analysis favours an uniform initial distribution for both the magnetic field (10^{10-13} G) and the spin period ($10-100$ ms). The implementation of radio selection effects is critical to match not only the spin period and period derivative, but also the orbital period and eccentricity of Galactic BNSs. According to our fiducial model, the Square Kilometre Array will detect $\sim$20 new BNSs in the Milky Way.

Key words: gravitational waves – methods: numerical – binaries: general – stars: neutron – pulsars: general.

1 INTRODUCTION

Radio pulsars are highly magnetized, rapidly spinning neutron stars (NSs) that emit beams of electromagnetic radiation, making them some of the most precise cosmic clocks known to science (Hewish et al. 1968; Pacini 1968). They can provide us with a wealth of information. Their spin period and spin period derivative can be measured with high accuracy. The timing precision of radio pulsars allows for tests of general relativity in the strong-field regime, which would otherwise be unfeasible with terrestrial laboratories. The only binary pulsar system known to date, PSR J0737-3039A/B (Burgay et al. 2003; Lyne et al. 2004), is a unique laboratory for tests of gravity theories and for the study of highly condensed matter (e.g. Kramer et al. 2006; Lattimer 2021). Moreover, the pulsar timing array (PTA; a set of pulsars which is analysed to search for correlated signatures in the pulse arrival times; Hobbs et al. 2010; Hobbs 2013; Manchester et al. 2013; Lentati et al. 2015; Arzoumanian et al. 2018; Miles et al.

2023) makes it possible to investigate the sources of low-frequency gravitational waves (GWs), such as supermassive black hole mergers (Arzoumanian et al. 2020).

The formation and evolution properties of pulsars are still matter of debate. Earlier efforts attempted to infer the birth distribution of pulsar properties from their observed Galactic population (Ostriker & Gunn 1969; Faucher-Giguère & Kaspi 2006), the main long-standing issue being that of magnetic field decay (Faucher-Giguère & Kaspi 2006). Based on a theoretical argument, magnetic field decay might generate from Ohmic dissipation, caused by the formation of electric currents on the NS crust (Bhattacharya et al. 1992; Konar & Bhattacharya 1997, 1999). This effect is probably more relevant, however, during accretion (Kiel et al. 2008). A number of magnetic field decay time-scales has been explored to date (Gonthier, Van Guilder & Harding 2004; Faucher-Giguère & Kaspi 2006; Kiel et al. 2008; Osłowski et al. 2011; Chattopadhyay et al. 2020, 2021). The understanding of pulsars birth properties might help to shed light on the supernova (SN) explosion mechanism, because we expect that the newly born NS properties are tightly correlated with the pre-SN star (Faucher-Giguère & Kaspi 2006; Kapil et al. 2023).

★ E-mail: cecilia.sgalletta@gmail.com (CS); giuliano.iorio@unipd.it (GI); mapelli@uni-heidelberg.de (MM)

The presence of a radio pulsar in a binary system allows us to measure the orbital properties (orbital period, eccentricity, and masses) to a high level of accuracy (Kaspi, Taylor & Ryba 1994; Stairs et al. 2002; Kramer et al. 2006, 2021; Lorimer 2008; Özel et al. 2016). Thanks to this property of radio pulsars, we have detected about a dozen of binary neutron stars (BNSs) in the Milky Way (MW), i.e. binary systems in which both components are NSs (Hulse & Taylor 1975; Burgay et al. 2003; Lyne et al. 2004; Martinez et al. 2015; Özel et al. 2016; Tauris et al. 2017). BNSs are loud sources of GWs (Burgay et al. 2003; Abbott et al. 2017a; Beniamini & Piran 2019; Pol, McLaughlin & Lorimer 2019; Abbott et al. 2020; Pol, McLaughlin & Lorimer 2020; Radice, Bernuzzi & Perego 2020; Thrane, Osłowski & Lasky 2020; Mandel & Broekgaarden 2022; Spera, Trani & Mencagli 2022), their merger powers short gamma-ray bursts (Goldstein et al. 2017; Abbott et al. 2017b; Murase et al. 2018; Colombo et al. 2022; Perna et al. 2022) and kilonovae (Tanvir et al. 2013; Kasen et al. 2017; Metzger 2017; Smartt et al. 2017; Troja et al. 2017; Metzger 2019; Nedora et al. 2023), and is a fundamental source of chemical enrichment by *r*-process elements (Eichler et al. 1989; Hotokezaka, Beniamini & Piran 2018; Côté et al. 2019; Combi & Siegel 2023; Fujibayashi et al. 2023; Kobayashi et al. 2023).

The formation of a BNS from the evolution of a massive binary star is still controversial (e.g. Tutukov & Yungel'Son 1993; Lipunov, Postnov & Prokhorov 1997; Portegies Zwart & Yungelson 1998; Beniamini & Piran 2016; Tauris et al. 2017; Belczynski et al. 2018; Chruslinska et al. 2018; Giacobbo & Mapelli 2018; Kruckow et al. 2018; Vigna-Gómez et al. 2018; Andrews & Mandel 2019; Neijssel et al. 2019; Belczynski et al. 2020; Chattopadhyay et al. 2020; Vigna-Gómez et al. 2020; Olejak, Belczynski & Ivanova 2021; Broekgaarden et al. 2022; Olejak et al. 2022; Riley et al. 2022; Iorio et al. 2023). According to the standard scenario, the two progenitor stars undergo at least one Roche-lobe overflow, after which the first SN takes place, leading to the formation of the first NS. If the binary system is tight enough to avoid disruption by the natal kick, the evolution of the companion star then initiates a common envelope (CE) phase, which results in the ejection of the envelope and the formation of a tight binary system composed of an NS and a naked He star. If such system avoids disruption even during the second SN, a BNS forms, which might then harden by GW emission until it reaches coalescence (Tauris et al. 2017, and references therein). An alternative scenario consists in a CE phase between the two progenitor stars (before the birth of the first NS), leading to the formation of a binary system composed of two naked cores on to a very tight orbit. Such binary system might avoid ionization during the two SN explosions and lead to the formation of a BNS (Brown 1995; Dewi, Podsiadlowski & Sena 2006; Justham, Podsiadlowski & Han 2011; Vigna-Gómez et al. 2018, 2020; Broekgaarden et al. 2021; Iorio et al. 2023).

Two of the most important unknowns of binary star evolution are the physics of CE (Ivanova et al. 2013; Klencki et al. 2021; Röpke & De Marco 2023) and the natal kick (Woosley 1987; Janka & Mueller 1994; Lai, Chernoff & Cordes 2001; Hobbs et al. 2005; O'Doherty et al. 2023). CE (Paczynski 1976; Webbink 1985) is usually described with a simple energy formalism, in which we assume that a fraction α of the kinetic orbital energy of the two cores is transferred to the envelope and helps unbinding it (see e.g. Nelemans et al. 2000; Hirai & Mandel 2022; Di Stefano et al. 2023, for alternative models). The distribution of natal kicks is often modelled with a Maxwellian curve with one-dimensional root mean square $\sigma = 265 \, \text{km s}^{-1}$, based on the proper motions of 73 young Galactic radio pulsars (Hobbs et al. 2005). However, core-collapse SN models suggest that the kick

might be much lower in presence of a stripped or ultra-stripped SN, i.e. an SN triggered by a naked He or CO core (Nordhaus et al. 2010, 2012; Tauris, Langer & Podsiadlowski 2015; Bray & Eldridge 2016; Tauris et al. 2017; Bray & Eldridge 2018; Giacobbo & Mapelli 2020; Coleman & Burrows 2022). Moreover, electron-capture SNe, especially in binary systems, might be associated with low kicks (Gessner & Janka 2018; Giacobbo & Mapelli 2019; Müller et al. 2019; Stevenson et al. 2022).

The aim of this work is to characterize the population of Galactic BNSs, by using a population synthesis code coupled with an MW model. We evolve the orbital binary properties, the spin period and magnetic field of pulsars. With this framework, we explore the merger rates, the orbital properties, and the population of radio pulsars. We consider many different assumptions for the MW model, the magnetic field, and the binary population parameters. We compare our models with current observations of Galactic BNSs.

To this purpose, we use the state-of-the-art population synthesis code SEVN (Spera & Mapelli 2017; Spera et al. 2019; Mapelli et al. 2020; Iorio et al. 2023) to implement single and binary stellar evolution. We adopt four MW models, employing semi-empirical prescriptions (Chiappini, Matteucci & Gratton 1997; Courteau et al. 2014; Pezzulli & Fraternali 2015; Grisoni et al. 2017; Boco et al. 2019) and cosmological simulations (Schaye et al. 2014; The EAGLE team 2017; Nelson et al. 2019a, b). We explore several parameters, such as α, the birth distribution of spin periods and surface magnetic fields of pulsars, the natal kick distribution, and the magnetic field decay time-scale. We test our results against the observed Galactic pulsar population.

2 METHODS

We study the Galactic BNS population by coupling various MW models with BNS catalogues obtained with the SEVN population synthesis code. Here below, we present the details of our models.

2.1 SEVN

The stellar evolution for *N*-body (SEVN) code is a state-of-the-art binary population synthesis code that implements single stellar evolution by interpolating pre-computed stellar tracks on the fly, and binary processes through analytic and semi-analytic models (Spera & Mapelli 2017; Spera et al. 2019; Mapelli et al. 2020). We use the latest version of the SEVN code, described in Iorio et al. (2023).[1] In the following, we will give a general overview of the main features of SEVN focusing on the processes most relevant for this work. We refer to Iorio et al. (2023) for a detailed description of the code. The first distinctive mark of SEVN is the way it handles single stellar evolution: the interpolation of look-up tables makes SEVN fast and versatile. In fact, it is possible to change stellar evolution models by simply substituting the input stellar track tables. The stellar tracks adopted in this work have been evolved with the PARSEC code[2] (Bressan et al. 2012; Costa et al. 2019; Costa et al. 2021; Nguyen et al. 2022).

SEVN includes several prescriptions for core-collapse SN explosions. In this work, we investigate the impact on our results of three of them: the *rapid* and *delayed* models by Fryer et al. (2012) and

---

[1] SEVN is publicly available at https://gitlab.com/sevncodes/sevn.git. The version used in this work is the release *Sgalletta23*: https://gitlab.com/sevncodes/sevn/-/releases/sgalletta23.

[2] We adopt the tables labelled *SEVNtracks_parsec_ov05_AGB* for the H-stars and *SEVNtracks_parsec_pureHe36* for the naked He stars.

the *rapid-Gauss* model. The rapid and the delayed models are both based on a convection-enhanced neutrino-driven mechanism for the SN explosion, though the revival of the shock wave happens within the first 250 ms after the collapse in the rapid model, whereas such time-scale can be much longer for the delayed model. The two prescriptions predict the masses of compact remnants as the sum of the mass of the proto-compact object and the amount of fallback material. The third model we adopted is based on the rapid explosion mechanism but draws the NS masses from a Gaussian distribution peaked at $1.33\,M_\odot$ with standard deviation $0.09\,M_\odot$, resulting from a fit to the Galactic BNS masses (Özel et al. 2012, 2016). We decided to introduce this model because both the rapid and delayed prescriptions fail to reproduce the observed NS mass distribution (Vigna-Gómez et al. 2018). In the delayed, rapid, and rapid-Gauss models, we do not allow for NS masses $<1.1\,M_\odot$. SEVN assumes that if a compact remnant has mass $\in [1.1, 3)\,M_\odot$ it is an NS, whereas if it has a mass $\geq 3\,M_\odot$ it is a black hole. The NS radius is fixed at 11 km (Özel et al. 2012; Bogdanov et al. 2016; Bauswein et al. 2017; Abbott et al. 2018).

SEVN includes several formalisms to model natal kicks. Here, we draw black hole natal kicks following Giacobbo & Mapelli (2020):

$$V_{\text{kick}} = f_{\text{H05}} \frac{\langle M_{\text{NS}} \rangle}{M_{\text{rem}}} \frac{M_{\text{ej}}}{\langle M_{\text{ej}} \rangle}, \tag{1}$$

where $\langle M_{\text{NS}} \rangle$ and $\langle M_{\text{ej}} \rangle$ are the average NS mass and ejecta mass from single stellar evolution, respectively, while M_{rem} and M_{ej} are the compact object mass and the ejecta mass (Giacobbo & Mapelli 2020). The term f_{H05} is a random number drawn from a Maxwellian distribution with one-dimensional root mean square $\sigma_{\text{kick}} = 265\ \text{km s}^{-1}$, coming from a fit to the proper motions of 73 young pulsars (<3 Myr) in the MW (Hobbs et al. 2005). In this formalism, stripped and ultra-stripped SNe result in lower kicks with respect to the other explosions, owing to the lower amount of ejected mass M_{ej} (Bray & Eldridge 2016, 2018). In Appendix A, we explore different assumptions for the natal kick and their impact on our main results. In addition to the natal kick, we also calculate a Blaauw kick (Blaauw 1961) resulting from the instantaneous mass-loss in a binary system triggered by an SN explosion. We use the same formalism as described in appendix A of Hurley, Tout & Pols (2002).

2.2 Binary evolution

In the following, we focus on the binary evolution processes implemented in SEVN that are relevant for this work, especially Roche-lobe overflow (RLO) and the CE phase (Iorio et al. 2023). The Roche lobe of a star in a binary system defines the region of space within which matter is gravitationally bound to the star itself. Therefore, when a star fills its Roche lobe, matter flows to the companion object under its gravitational attraction. This process is known as RLO. RLO thus involves variations in the mass ratio, in the masses and radii of the two stars and in the semimajor axis of the system. At each time-step, SEVN evaluates the Roche-lobe radius of the two stars in the binary system using the analytical expression derived in Eggleton (1983):

$$\frac{R_L}{a} = \frac{0.49\, q^{2/3}}{0.6 q^{2/3} + \ln(1 + q^{1/3})}, \tag{2}$$

where q is the mass ratio and a is the semimajor axis. If either star radii satisfy the condition $r \geq R_L$, a RLO episode initiates and mass falls from the donor (the star filling its Roche lobe) to the accretor. Depending on the response of the Roche-lobe and donor radius to mass stripping, mass transfer can be stable or unstable. To assess the stability of mass transfer, SEVN adopts a formalism common to many

population synthesis codes (see e.g. Hurley et al. 2002; Hobbs et al. 2005). The mass ratio of the donor d star to the accretor a star, q, is compared to a critical value q_c, dependent on the stellar evolutionary phase of the donor star: if $q > q_c$ the mass transfer is unstable on a dynamical time-scale. Here, we use the values of q_c adopted in the fiducial simulations of Iorio et al. (2023, see their table 3). In this model, mass transfer is always stable if the donor star is in the main sequence or in the Hertzprung gap evolutionary phase. In the case of stable mass transfer, the mass-loss rate in SEVN scales as Hurley et al. (2002)

$$\dot{M}_{\text{d}} = -F(M_{\text{d}}) \left(\ln \frac{R_{\text{d}}}{R_{\text{L,d}}} \right)^3 \, M_\odot\, \text{yr}^{-1}, \tag{3}$$

where $F(M_{\text{d}})$ is a normalization factor, R_{d} is the radius of the donor, and $R_{\text{L,d}}$ is the Roche lobe of the donor star. SEVN allows for non-conservative mass transfer; therefore, the mass lost by the donor can be bigger than the amount accreted by the companion. The mass accreted is modelled as follows:

$$\dot{M}_{\text{a}} = \begin{cases} \min{(\dot{M}_{\text{Edd}}, \, -f_{\text{MT}}\, \dot{M}_{\text{d}})} & \text{if the accretor is a compact object} \\ -f_{\text{MT}}\, \dot{M}_{\text{d}} & \text{otherwise,} \end{cases} \tag{4}$$

where $\dot{M}_{\text{Edd}}$ is the Eddington rate and $f_{\text{MT}} \in [0, 1]$ is the mass accretion efficiency. We set $f_{\text{MT}} = 0.5$ in our simulations (Bouffanais et al. 2021; Iorio et al. 2023).

When mass transfer is unstable the outcome can be either a stellar merger or a CE. During the CE phase, the cores of the two stars orbit each other within a shared envelope. SEVN parametrizes the CE phase using the α formalism (Webbink 1985; Tout et al. 1997). The envelope's binding energy at the onset of the CE is evaluated as

$$E_{\text{bind,i}} = -G \left(\frac{M_1 M_{\text{env,1}}}{\lambda_1 R_1} + \frac{M_2 M_{\text{env,2}}}{\lambda_2 R_2} \right), \tag{5}$$

where M is the mass of the star, M_{env} is the mass of the envelope, and R is the star's radius. The subscripts 1 and 2 refer to the primary and secondary star, respectively. Finally, λ takes into account the structural properties of the envelope of each star, which is calculated following the model by Claeys et al. (2014), as described in appendix A of Iorio et al. (2023). The variation of the orbital energy is

$$\Delta E_{\text{orb}} = \frac{G M_{\text{c,1}} M_{\text{c,2}}}{2} \left(a_{\text{f}}^{-1} - a_{\text{i}}^{-1} \right), \tag{6}$$

where $M_{\text{c,1}}$ and $M_{\text{c,2}}$ are the core masses of the two stars and a_{i} and a_{f} are the semimajor axis at the onset and at the end of the CE, respectively. SEVN infers the values of a_{f} through the condition $E_{\text{bind,i}} = \alpha \Delta E_{\text{orb}}$. The α parameter represents the efficiency of energy transport from the binary orbit to the envelope. According to its original definition, α should take values between 0 and 1, but recently values of $\alpha > 1$ have been explored, to account for the missing physics in this very simplified formalism (e.g. Fragos et al. 2019). If the core radii of the two stars are both smaller than their Roche lobes at the end of CE (equation 2), then the envelope is ejected. Otherwise, the two stars merge during the CE phase.

2.3 NS properties

To study the evolution of the physical properties of NSs with SEVN, at the time of formation we assign to each NS a spin, a magnetic field and an angle between the rotation and the magnetic axis, α_{B}. For all of our NSs, we generate $\cos\alpha_{\text{B}}$ from an uniform distribution between 0 and 1. The evolution of each NS depends on its interaction with the companion star. If the NS is not accreting matter from the

companion, the evolution is the same as if the NS were isolated, i.e. the NS spin and magnetic field decrease with time (*spin down*). In contrast, if the companion star fills its Roche lobe, the infalling matter can transfer angular momentum to the NS, causing the latter to spin up. When the latter process takes place the resulting NS is said to be *recycled*. In fact, observed recycled pulsars are usually characterized by short spin periods and relatively low magnetic fields (Lorimer 2008; Lorimer 2011; Özel et al. 2016).

2.3.1 Spin down

If the evolution of the pulsar proceeds unperturbed, the pulsar can be seen as a rotating magnet. We model the magnetic field of the pulsar with a dipole and compute the loss of energy accordingly. In fact, as the pulsar rotates it emits electromagnetic radiation, losing rotational energy, that is the pulsar spins down. The angular frequency of the pulsar changes according to Goldreich & Julian (1969):

$$\dot{\Omega} = -\frac{8\,\pi\,B^2\,R^6\,\sin^2\alpha_B\,\Omega^3}{3\,\mu_0\,c^3\,I}, \tag{7}$$

where Ω is the angular frequency, B is the surface magnetic field, R is the radius, α_B is the angle between the rotational axis and the magnetic axis, I is the moment of inertia of the pulsar, c is the speed of light, and μ_0 is the vacuum magnetic permeability. The time derivative of the angular frequency $\dot{\Omega}$ is linked to Ω through the relation $\dot{\Omega} \propto \Omega^n$, where n is the magnetic braking index. Observational evidence points towards a value of n lying in the range of $2.5-3.5$ (Manchester et al. 2005). In addition, we assume that the magnetic field decays with time because of Ohmic dissipation. The finite resistivity in the NS crust, caused by electron scatterings, converts the magnetic energy into heat (Goldreich & Reisenegger 1992; Konar & Bhattacharya 1997; Urpin & Konenkov 1997; Konar & Bhattacharya 1999). Furthermore, observations seem to support the decay of the magnetic field: younger pulsars show in general stronger magnetic fields with respect to older ones (Ostriker & Gunn 1969). In our models, we evolve the magnetic field following an exponential decay (Kiel et al. 2008; Osłowski et al. 2011; Chattopadhyay et al. 2020, 2021):

$$B = (B_0 - B_{\min})\,e^{-t/\tau_d} + B_{\min}, \tag{8}$$

where B_0 is the initial surface magnetic field, $B_{\min}$ is the minimum surface magnetic field strength, and τ_d is the magnetic field decay time-scale. We assume that the pulsar magnetic field stops decreasing when it reaches the value $B_{\min}$. Throughout this work, we adopt $B_{\min} = 10^8$ G, as suggested by Zhang & Kojima (2006). The magnetic field decay time-scale τ_d is a free parameter of the model. Its value is controversial: ranging from 2–5 Myr (e.g. Osłowski et al. 2011) to 2000 Myr (e.g. Kiel et al. 2008). Faucher-Giguère & Kaspi (2006) carry out their analysis considering no magnetic field decay at all.

Following Chattopadhyay et al. (2020), we get an analytic expression for the evolution of the angular frequency of the pulsar:

$$\frac{1}{\Omega_f^2} = \frac{1}{\Omega_i^2} + \frac{16\,\pi\,R^6\,P\,\sin^2\alpha_B}{3\,\mu_0\,c^3\,I}$$
$$\times \left[B_{\min}^2\,\Delta t - \tau_d\,B_{\min}(B_f - B_i) - \frac{\tau_d}{2}(B_f^2 - B_i^2) \right], \tag{9}$$

where Ω_i and Ω_f are the initial and final angular frequencies, B_i and B_f are the initial and final magnetic fields, and Δt is the time elapsed between the final and the initial states.

The spin period P and the spin down rate $\dot{P}$ can then be obtained from Ω and $\dot{\Omega}$ through the following relations:
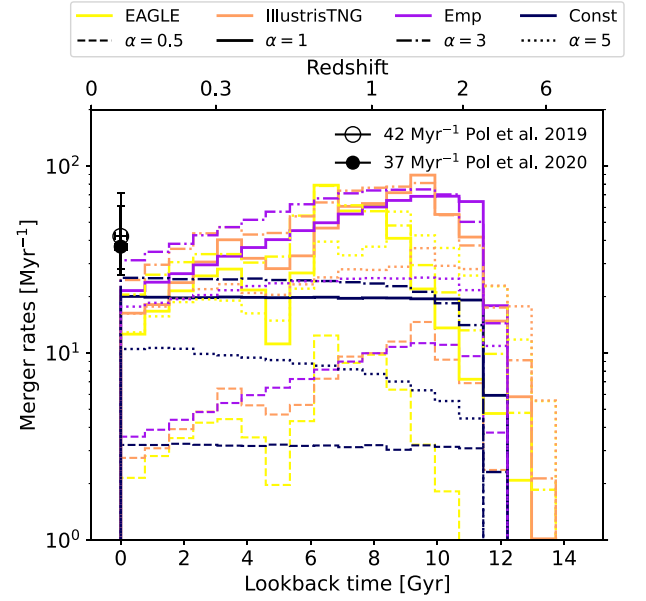
Figure 1. BNS merger rate in the MW as a function of the look-back time for different Galaxy models and values of the CE parameter α. Each colour identifies a Galaxy model. Yellow: EAGLE; pink: ILLUSTRISTNG; purple: Emp; blue: Const. Each line-style is associated with a value of α. Dashed line: $\alpha = 0.5$; solid line: $\alpha = 1$; dash–dotted line: $\alpha = 3$; dotted line: $\alpha = 5$. The circles show the BNS merger rate in the MW inferred from observations: the unfilled circle shows the value by Pol et al. (2019), $\mathcal{R}_{MW} = 42^{+30}_{-14}$ Myr^{-1}; the black filled circle shows the updated value by Pol et al. (2020), $\mathcal{R}_{MW} = 37^{+24}_{-11}$ Myr^{-1}. All simulations shown in this figure assume $\tau_d = 1$ Gyr and the U distribution for initial spins and magnetic fields. We do not expect NS spins and magnetic fields to affect the merger rate. Our fiducial model (Ua3t1Emp, Table 3) produces a rate $\mathcal{R}_{MW} = 31.3$ Myr^{-1}, consistent with the rate inferred from the Galactic pulsar binary systems.

$$P = \frac{2\,\pi}{\Omega}, \tag{10}$$

$$\dot{P} = -\frac{\dot{\Omega}\,P}{\Omega}. \tag{11}$$

We update the values of the NS spin periods and magnetic fields in SEVN after each time-step according to equations (8) and (9). We can trace the pulsar evolution in the $P-\dot{P}$ diagram. Because of spin down, pulsars evolve towards larger spin periods and lower magnetic fields. In the $P-\dot{P}$ plane, this trend results in a diagonal shift, towards the lower right corner of the plot (see e.g. fig. 2 in Chattopadhyay et al. 2020). The time-scale of this evolution depends on the choice of τ_d: for shorter values of τ_d the traversal of the $P-\dot{P}$ plane is faster.

2.3.2 Spin up

Matter exchange processes in binary stars, such as those happening during a RLO, can significantly affect the evolution of NS spin and magnetic field. For instance, part of the angular momentum of the exchanged material, can be transferred to the NS, that, consequently, spins up. In SEVN, we have implemented the spin-up process of NSs during RLO mass transfer following the same prescriptions as in Kiel et al. (2008) and Chattopadhyay et al. (2020). The rate of change in the angular momentum of the pulsar $\dot{J}_{acc}$ scales linearly with the amount of accreted mass, that is:

$$\dot{J}_{acc} = \epsilon\,V_{diff}\,R_A^2\,\dot{M}_{NS}, \tag{12}$$
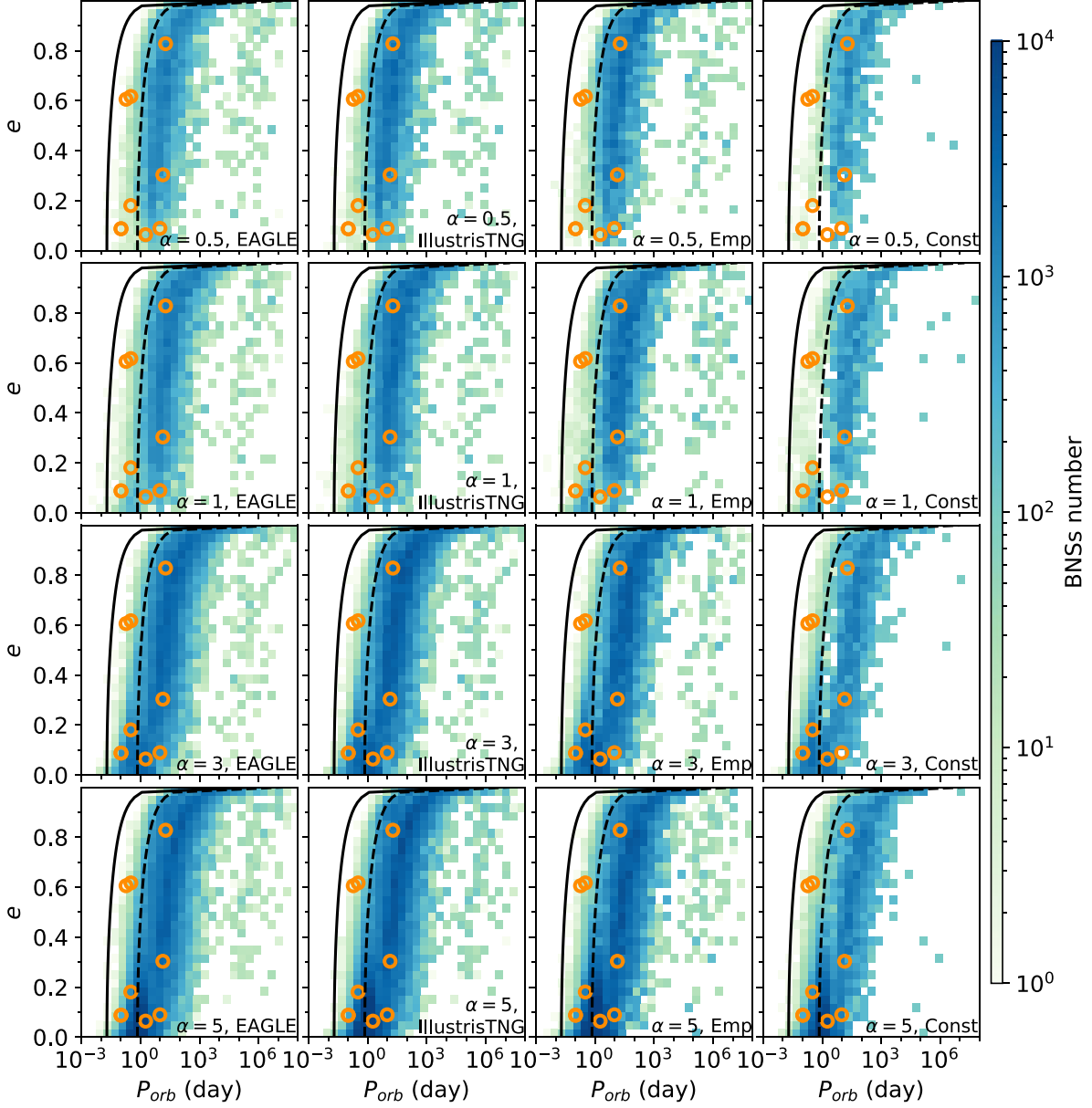
Figure 2. Distribution of the simulated BNSs at the present time in the $P_{orb}-e$ plane. Each column shows the results for a different Galaxy model, from left to right: EAGLE, ILLUSTRISTNG, Emp and Const. The rows show different α values, from top to bottom: $\alpha = 0.5$, 1, 3, and 5. All the models shown here assume $\tau_d = 1$ Gyr, and model U for the initial spin and magnetic field. The red circles show the observed population of BNSs selected for this study. The solid black line shows values of constant $t_{GW} = 1$ Myr, while the dashed black line corresponds to t_{GW} equal to the Hubble time. We obtained the lines of constant t_{GW} with equation D6 in Iorio et al. (2023),[3] assuming a mass of 1.35 $M_\odot$ for the NSs. Our models qualitatively agree with the observed BNS distribution.

where ϵ is an efficiency factor, set at 1 in our models, $\dot{M}_{NS}$ is the mass accretion rate on the NS, and R_A is the magnetic radius. We define $R_A = R_{Alfven}/2$. The Alfven radius R_{Alfven} is the radius at which the magnetic pressure equals the ram pressure:

$$R_{Alfven} = \left(\frac{2\,\pi^2}{G\,\mu_0^2}\right)^{1/7} \times \left(\frac{R^6}{\dot{M}_{NS}\,M_{NS}^{1/2}}\right)^{1/7} \times B^{4/7}. \qquad (13)$$

V_{diff} is the difference between the Keplerian angular velocity at the magnetic radius $\Omega_K|_{R_A}$ and the co-rotation angular velocity Ω_{co}:

$$V_{diff} = \Omega_K|_{R_A} - \Omega_{co}. \qquad (14)$$

We can see from equation (12), that the condition for the NS to spin up is $V_{diff} > 0$. In this case, the variation in angular momentum of the NS is positive and its spin increases: as matter reaches the magnetic radius, the magnetic pressure dominates and matter follows the magnetic field lines and is accreted on the NS polar caps. In contrast, if $V_{diff} < 0$, then the NS acts as a propeller (Kiel et al. 2008): the velocity of the magnetic field lines at the magnetic radius is higher than the local Keplerian velocity ($\Omega_{co} > \Omega_K|_{R_A}$) and matter is blown away from the NS (Illarionov & Sunyaev 1975). In SEVN, we have implemented the propeller effect as well.

We also assume that the magnetic field decays exponentially with the amount of mass accreted. Observations of the low magnetic

fields of binary and millisecond pulsars suggest accretion-induced field decay (Konar & Bhattacharya 1997). The magnetic field evolves according to the following equation during RLO in our models:

$$B = (B_0 - B_{\min}) \times \exp\left(-\frac{\Delta M_{\rm NS}}{\Delta M_{\rm d}}\right) + B_{\min}. \tag{15}$$

$\Delta M_{\rm NS}$ is the amount of mass accreted by the NS and $\Delta M_{\rm d}$ is the magnetic field decay mass scale, another free-parameter of the model. We fixed $\Delta M_{\rm d}$ to the fiducial value $\Delta M_{\rm d} = 0.025\,{\rm M}_\odot$, which corresponds to the optimal value obtained in Chattopadhyay et al. (2020). We further discuss the values adopted in our simulations in Section 2.7.

At each time-step, SEVN evaluates if matter accretes on to the NS via RLO. If not, the variations to the spin and magnetic field of the NS are only due to spin down (equations 7 and 8). Otherwise, the algorithm first evaluates $V_{\rm diff}$. If $V_{\rm diff} > 0$, SEVN calculates also the spin up from equations (12) and (15):

$$\Omega_{\rm i+1} = \Omega_{\rm i} + \frac{\Delta J_{\rm acc}}{I}, \tag{16}$$

where $\Delta J_{\rm acc} = V_{\rm diff}\, R_{\rm A}^2 \Delta M_{\rm NS}$. At the end of the time-step, SEVN updates both the spin and the magnetic field accordingly. If $V_{\rm diff} < 0$, no matter accretes during that time-step and spin and magnetic fields are updated only accounting for spin down. This accurate treatment of spin up and down benefits from the adaptive time-step formalism of SEVN (Iorio et al. 2023).

According to Chattopadhyay et al. (2020), a CE phase can trigger further spin up of the NS, as suggested by MacLeod & Ramirez-Ruiz (2015). Here, we decide not to include this possible spin up by CE, because it is quite controversial (Osłowski et al. 2011; Chamandy et al. 2018).

2.4 Initial conditions for the SEVN binary catalogues

We sample the masses of the primary stars (M_1) from a Kroupa's initial mass function (Kroupa 2001), in a range between 5 and 150 M$_\odot$:

$$\mathcal{F}(M) \propto M_1^{-2.3}. \tag{17}$$

We draw the secondary star's mass (M_2), the initial binary orbital period ($P_{\rm orb}$), and the eccentricity following the distributions derived by Sana et al. (2012), which are based on observations of massive binary stars in young clusters:

$$\mathcal{F}(q) \propto q^{-0.1}, \tag{18}$$

where $q = M_2/M_1 \in [q_{\min}, 1]$, $q_{\min} = \max\left(\frac{2.2{\rm M}_\odot}{M_1}, 0.1\right)$, so that the secondary star mass distribution is cut at 2.2 M$_\odot$,

$$\mathcal{F}(P_{\rm orb}) \propto (\log P_{\rm orb})^{-0.55} \tag{19}$$

with $0.15 \leq \log(P_{\rm orb}/d) \leq 5.5$, and

$$\mathcal{F}(e) \propto e^{-0.42} \tag{20}$$

with $0 \leq e \leq 0.9$. For each parameter (described in Section 2.7), we simulate with SEVN 11 subsets varying the metallicity: $Z = 0.0002$, 0.0004, 0.0008, 0.0012, 0.0016, 0.002, 0.004, 0.008, 0.012, 0.016, 0.02. Each SEVN sub-set evolves 10^6 binary systems. Therefore, for each model we ran a total of 1.1×10^7 binaries.

2.5 MW models

In our work, we couple the catalogues of binary NS systems from SEVN with a MW-like galaxy. We choose four Galaxy models that

Table 1. Properties of the MW models. Columns 1 and 2 refer to the total stellar mass $M_\star$ and current SFR of the considered Galaxy models.

MW model	$M_\star$ (10^{10} M$_\odot$)	SFR (M$_\odot$ yr^{-1})
EAGLE	3.7	1.38
ILLUSTRISTNG	5.1	1.67
Empirical (Emp)	5.0	1.65
Constant (Const)	1.9	1.65

have total stellar mass and current SFR as close as possible to the measured values of the MW (Artale et al. 2019). Therefore, we require a total stellar mass $(5.43 \pm 0.57) \times 10^{10}$ M$_\odot$ (McMillan 2017) and a current SFR ~ 1.65 M$_\odot$ yr^{-1} (Licquia & Newman 2015). The use of different Galaxy models allows us to test the robustness of our results against the specific features of the chosen MW models. Here below, we describe the four models in detail. We summarize them in Table 1.

2.5.1 Constant SFR (const model)

The first model for the MW assumes a constant SFR, fixed at 1.65 M$_\odot$ yr^{-1}. All binary systems in this model have solar metallicity, $Z = 0.0142$ (Asplund et al. 2009; Vigna-Gómez et al. 2018; Chattopadhyay et al. 2020). The integration of the SFR through cosmic time leads to a total stellar mass $M_\star \sim 1.9 \times 10^{10}$ M$_\odot$, well below the observed value. This MW model has been used by most of the previous works (e.g. Shao & Li 2018; Vigna-Gómez et al. 2018; Chattopadhyay et al. 2020), adopting a fixed SFR at 1 M$_\odot$ yr^{-1}.

2.5.2 The EAGLE model

The EAGLE project[4] (Schaye et al. 2014; The EAGLE team 2017) comprises a set of cosmological hydrodynamical simulations with comoving box sizes of 25, 50, and 100 Mpc, evolved from redshift $z = 20$ to $z \sim 0$. The simulations are run with the GADGET-3 code (Springel 2005). A full description of the sub-grid baryonic processes included can be found in Schaye et al. (2014). The cosmological framework adopted is the Lambda cold dark matter (ΛCDM) cosmological model, with cosmological parameters: $\Omega_{\Lambda,0} = 0.693$, $\Omega_{\rm M,0} = 0.307$, $\Omega_{\rm b,0} = 0.048$, $\sigma_8 = 0.8288$, $n_s = 0.9611$, and $h = 0.6777$ (Ade et al. 2014). We selected a MW-like galaxy from the EAGLE run labelled L025N0752, characterized by a periodic box of side 25 Mpc comoving. This is the run with the highest resolution in the EAGLE suite: the baryonic particle and the dark matter mass resolutions are 2.26×10^5 and 1.21×10^6 M$_\odot$, respectively. By imposing the requirements outlined in Section 2.5, we selected a best-fitting galaxy identified by the IDs of the halo, Gnr = 23 and the sub-halo, Sgrn = 0. This galaxy is characterized by a total stellar mass 3.65×10^{10} M$_\odot$ and a current SFR 1.38 M$_\odot$ yr^{-1}.

2.5.3 The ILLUSTRISTNG model

The ILLUSTRISTNG project[5] consists of three simulation volumes, with comoving box size of 50, 100, and 300 Mpc, from redshift $z = 127$ to $z \sim 0$. The simulations have been run with the moving mesh code AREPO (Springel 2010). A full description of the baryonic processes included in this simulation can be found in Nelson et al.

[4] https://icc.dur.ac.uk/Eagle/
[5] https://www.tng-project.org/

(2019a) and Pillepich et al. (2019). A ΛCDM cosmological model is assumed, with cosmological parameters from Ade et al. (2016): $\Omega_{\Lambda,0} = 0.6911$, $\Omega_{M,0} = 0.3089$, $\Omega_{b,0} = 0.0486$, $\sigma_8 = 0.8159$, $n_s = 0.9667$, and $h = 0.6774$. We select our MW-like galaxy from the TNG50 run (with 50 Mpc comoving length, Nelson et al. 2019b). The best candidate galaxy for our work is identified by Gnr = 244 and Sgrn = 547844, with a total stellar mass 5.10×10^{10} M$_\odot$ and current SFR 1.675 M$_\odot$ yr^{-1}. The galaxy is included in the MW-type catalogue released by Pillepich et al. (2023) from the TNG50 simulation.

2.5.4 The empirical (Emp) model

We also include a MW-like model built from empirical relations. We adopt an exponentially decaying SFR function:

$$\text{SFR}(\tau) = A \exp(-\tau/\tau_\Psi), \tag{21}$$

where A is a proportionality constant, τ is the internal Galactic age, defined as the time t_f elapsed since the beginning of significant star formation activity in the Galaxy, and τ_Ψ is the characteristic timescale for the suppression of SFR (Bovy 2017; Grisoni et al. 2017; Boco et al. 2019). This model is commonly adopted to describe low-redshift, disc-dominated galaxies (Chiappini et al. 1997; Courteau et al. 2014; Pezzulli & Fraternali 2015; Grisoni et al. 2017). Integrating the SFR over the cosmic time yields the total stellar mass of the galaxy:

$$M_\star(t_0) = \int_{t_f}^{t_0} \text{SFR}(t)\, dt, \tag{22}$$

where t_0 is the cosmic time today. For our MW-like galaxy, we set $\tau_\Psi = 7$ Gyr, as the SFR decay time-scale (Bovy 2017). To derive the two unknowns in equations (21) and (22), A and t_f, we imposed a total stellar mass $M_\star(t_0) = 5 \times 10^{10}$ M$_\odot$ and a current star formation rate SFR$(t_0) = 1.65$ M$_\odot$ yr^{-1}.

As for the metallicity evolution, we assume the fundamental metallicity relation (FMR; Mannucci et al. 2010; Mannucci, Salvaterra & Campisi 2011). The FMR has been obtained empirically through observations of the local galaxies of the Sloan Digital Sky Survey, and its robustness has been confirmed for galaxies up to $z \sim 3.5$ (Mannucci et al. 2010; Hunt et al. 2016). The FMR links $M_\star$, SFR and the gas metallicity Z, whereas it is almost independent of redshift (Boco et al. 2021; Chruślińska et al. 2021; Santoliquido et al. 2022). Following this approach, the Galaxy metallicity is evaluated through equation 2 of Mannucci et al. (2011):

$$
12 + \log(\text{O/H})
$$
$$
= \begin{cases}
8.90 + 0.37\,m - 0.14\,s - 0.19\,m^2 \\
\quad + 0.12\,m\,s - 0.054\,s^2 & \text{for} \quad \mu_{0.32} \geq 9.5 \\
8.93 + 0.51\,(\mu_{0.32} - 10) & \text{for} \quad \mu_{0.32} < 9.5
\end{cases} \tag{23}
$$

with $\mu_{0.32} = \log M_\star - 0.32 \log \text{SFR}$, $m = \log M_\star - 10$, and $s = \log \text{SFR}$. We build our empirical model by evaluating the SFR (equation 21) and the metallicity at a series of time-steps, ranging from ~ 12 Gyr ago until today. At each time-step, we assume that the metallicity follows a log-normal distribution within the Galaxy, with mean equal to the value predicted by the FMR (equation 23) and variance $\sigma_{\log Z} = 0.1$ dex.

2.6 Populating the MW with BNSs

To populate the MW galaxy models with the catalogues of BNSs evolved with SEVN, we follow the same procedure as outlined in

Mapelli et al. (2017) and Mapelli & Giacobbo (2018). For each simulation set, we read the eccentricity e and the semimajor axis a of the binary, the times of the SN explosions t_1 and t_2, the NS masses m_1 and m_2, the spin periods P_1 and P_2 and magnetic fields B_1 and B_2 at the formation of the second compact object. Along with this, we save the total simulated initial stellar mass M_{SEVN} for each of the 11 metallicity sub-sets.

For the EAGLE and ILLUSTRISTNG models, we read every stellar particle from the snapshot of the Galaxy at redshift $z = 0$. In particular, we need the stellar particle mass $m_\star$, its formation redshift $z_\star$, and its metallicity at formation $Z_\star$. For each stellar particle, we select the SEVN catalogue with the metallicity closest to $Z_\star$, and associate it with a number of BNSs proportional to the ratio $m_\star/M_{\text{SEVN}}$:

$$n_{\text{BNS}} = N_{\text{SEVN}} \frac{m_\star}{M_{\text{SEVN}}} f_{\text{corr}}\, f_{\text{bin}}, \tag{24}$$

where N_{SEVN} is the number of BNSs within the selected catalogue, f_{corr}, and f_{bin} are correction factors. The factor $f_{\text{corr}} = 0.285$ takes into account that we consider only systems with primary star mass ≥ 5 M$_\odot$. By integrating the Kroupa IMF between 0 and 5 M$_\odot$, we obtain the relative weight of stars with a mass ≥ 5 M$_\odot$: this yields $f_{\text{corr}} = 0.285$. The factor f_{bin} corrects for the binary fraction, i.e. takes into account that we evolve only binary systems. From Sana et al. (2012), $f_{\text{bin}} = 0.4$, which is equivalent to saying that 40 per cent of stellar mass lie in binary systems. We randomly choose, with a Monte Carlo-like approach, n_{BNS} BNSs from the SEVN catalogue.

For the empirical model, we do not have stellar particles, but we can derive the amount of stellar mass formed by the Galaxy $\Delta M_\star$ at each time-step. Knowing the metallicity distribution at the same time-step, we can derive how much mass has been accreted $\Delta m_\star|_Z$, for each of the SEVN metallicities. The sum over all the 11 metallicities is

$$\Delta m_\star = \sum_{i=1}^{11} \Delta m_\star|_{Z_i}. \tag{25}$$

So, for each metallicity we evaluate n_{BNS} simply by substituting the value of $\Delta M_\star|_{Z_i}$ in equation (24).

We convert the formation redshift $z_\star$ of each stellar particle in look-back time:

$$t_{\text{lb}}(z) = \frac{1}{H_0} \int_0^z \frac{dz'}{(1+z')\sqrt{\Omega_{M,0}\,(z'+1)^3 + \Omega_{\Lambda,0}}} \tag{26}$$

choosing the cosmological parameters consistently with the adopted cosmological simulation (Section 2.5). Then, the formation time of a BNS within the Galaxy is[6]

$$t_{\text{BNS}} = t_\star - \max(t_1, t_2), \tag{27}$$

where $t_\star$ is the look-back time of the formation of the stellar particle corresponding to the redshift $z_\star$. From now on, all the times will be expressed in look-back times.

We assume that the subsequent evolution is driven only by the emission of GW radiation. Integrating the differential equations for GW radiation, derived in Peters (1964), we evolve the semimajor

---

[6]t_1 and t_2 mark the SN explosion times of the primary and secondary progenitor stars, respectively. An episode of mass transfer during the evolution of the system might revert the initial mass ratio, thus leading to $t_1 > t_2$.

axis a and the eccentricity e:

$$\frac{da}{dt} = -\frac{64}{5} \frac{G^3 \, m_1 \, m_2 (m_1 + m_2)}{c^5 \, a^3 \, (1 - e^2)^{7/2}} \left(1 + \frac{73}{24} e^2 + \frac{37}{96} e^4 \right),$$

$$\frac{de}{dt} = -\frac{304}{15} \frac{G^3 \, m_1 \, m_2 \, (m_1 + m_2)}{c^5 \, a^3 \, (1 - e^2)^{5/2}} \left(1 + \frac{121}{304} e^2 \right). \quad (28)$$

For the integration, we employ an Euler method with an adaptive time-step: the time-steps are smaller if the system is rapidly evolving (i.e. close to the merger); if the system is instead on a loose-wide orbit, the integration time-steps are larger. This allows us to have a fast algorithm without losing in precision. We evolve each system from t_{BNS} until today, i.e. $t_{lb} = 0$. If, during the evolution $a = 3 \, r_S$, where r_S is the Schwartzschild radius, we assume that the system has merged and do not evolve it anymore.

In parallel, we evolve the NS spin and magnetic field. In particular, we update the spin and magnetic field according to equations (8) and (9), with

$$\Delta t = t_{BNS} - t_{BNS, final}, \quad (29)$$

where $t_{BNS, final} = t_{merge}$ if the system has merged, or $t_{BNS, final} = 0$ (i.e. the present time) otherwise. We repeat the same procedure for each parameter set and for each Galaxy model keeping track of both the set of merged BNSs and the population of BNSs today in the MW.

2.7 Simulation set-up

We varied several parameters in our model: the SN explosion mechanism prescription (rapid, delayed, rapid-gauss), the CE efficiency parameter α ($\alpha = 0.5, 1, 3$, and 5), the initial spin and magnetic-field distributions, and the magnetic field decay time-scale τ_d. All the models adopt the rapid-gauss prescription to reproduce the masses of the NSs. In the Appendix B, we test for comparison also the rapid and the delayed models from Fryer et al. (2012). We investigate different values of the parameter α. In particular, we set $\alpha = 0.5, 1, 3$, and 5. Both spins and magnetic fields are drawn from initial distributions. We need to make this assumption because the link between the properties of the pre-SN star and those of the NS is highly uncertain. Given the small sample of observed pulsars, the initial distributions are still quite uncertain. There is no agreement in the literature on the favoured initial parameter distributions, see e.g. Faucher-Giguère & Kaspi (2006) and Osłowski et al. (2011). In our work, we consider the initial distributions as free parameters and test some of the most common models in the literature, as summarized in Table 2:

(i) *Uniform* (hereafter, U): The spin period and the magnetic field are drawn uniformly in the range [10, 100] ms and [10^{10}, 10^{13}] G, respectively.

(ii) *Flat-in-log* (hereafter, FL): The spin periods are drawn uniformly between 10 and 100 ms, the magnetic fields are distributed according to a flat-in-log distribution in the range [10^{10}, 10^{13}] G.

(iii) *Faucher-Giguère* (hereafter, FG): Spin periods and magnetic fields follow the distributions presented in Faucher-Giguère & Kaspi (2006). The spin periods follow a normal distribution with mean $\langle P \rangle = 300$ ms and variance $\sigma_P = 150$ ms, while the magnetic fields are drawn from a lognormal distribution with mean $\langle \log(B/G) \rangle = 12.65$ and variance $\sigma_{\langle \log B \rangle} = 0.55$.

Moreover, we consider different values for the magnetic field decay time-scale τ_d (equation (8)): $\tau_d = 0.1, 0.5, 1$, and 2 Gyr. We test our results on the different MW-like galaxies as well (Section 2.5). We adopt a uniform terminology for our models. Every model is identified with a string built as follows: '{distr}a{alpha}t{tau}{MW}',

where within the brackets we substitute the actual value (or acronym) assumed by that specific parameter in the model. So that, in the place of 'distr' we substitute the acronym for the initial spins and magnetic fields distributions (see Table 2); 'alpha' corresponds to the value α for CE efficiency, 'tau' represents the value τ_d of the magnetic field decay time-scale, and lastly 'MW' the MW-like galaxy chosen. We use the following abbreviations for the MW models: EAGLE, ILLUS-TRISTNG, Emp, and Const. For example, model 'Ua3t1Emp' adopts the uniform distribution of initial spin and magnetic field, $\alpha = 3$, $\tau_d = 1$ Gyr, and the empirical MW model. The models are summarized in Table 3. We choose 'Ua3t1Emp' as our fiducial model.

2.8 Selection effects

To compare our modelled BNSs with observations, we need to account for selection effects. For instance, as a pulsar crosses the death line (see Section 2.8.1) it ceases to emit in the radio. Furthermore, pulsars have quite narrow beaming opening angles, thus we can only detect the pulsars whose beam intersects the line of sight. Radio selection effects also depend on the sky location of the source. The flux density scales as the inverse of the distance squared, which means that, for a given intrinsic luminosity, observations are biased towards close pulsars. Moreover, scattering by free electrons in the interstellar medium smears the pulsars' signal, lowering the signal-to-noise ratio (Cordes & Lazio 2002). Other effects that may affect the observations are pulse nulling and intermittency, i.e. when the pulsed emission ceases for many pulse periods and quasi-periodic on/off cycles, respectively (Lyne et al. 2010). On top of this, the Doppler shifting of the period caused by orbital motion also smears the pulsar signal (Andersen & Ransom 2018; Balakrishnan et al. 2022). We use the PYTHON implementation of PSRPOP (Lorimer 2011) and PSRPOPPY[7] (Bates et al. 2014), to account for some of the mentioned selection effects. Specifically, we model the death lines and beam geometry, the dependence on sky location, interstellar radio scintillation, pulsar luminosity, and binary selection effects.

2.8.1 Death lines

Pulsars cease to emit in the radio when the magnetic field is not strong enough for the production of electron–positron pairs. The death lines, empirical relations in the P–$\dot{P}$ plane, mark the locus of points beyond which the pulsars stop emitting: if a pulsar crosses one of these lines in the P–$\dot{P}$ plane, it turns off. We adopt the death lines from Rudak & Ritter (1994):

$$\log \dot{P} = 3.29 \log P - 16.55$$
$$\log \dot{P} = 0.92 \log P - 18.65. \quad (30)$$

Moreover, to avoid the piling up of pulsars at the death lines, we also add a cut-off on the efficiency of radio emission as in Szary et al. (2014). The radio efficiency ξ_R is defined as

$$\xi_R = \frac{L}{\dot{E}}, \quad (31)$$

where L is the pulsar radio luminosity and $\dot{E} = 4 \pi^2 \, I \, P^{-3} \, \dot{P}$ is the pulsar spin down power. Following the model by Szary et al. (2014), if the radio efficiency exceeds a certain threshold ($\xi_R > \xi_{R,max}$), the pulsar ceases to emit. We set the threshold to $\xi_{R,max} = 0.01$, as in Chattopadhyay et al. (2020, 2021). Following these prescriptions,

[7]https://github.com/samb8s/PsrPopPy

Table 2. Initial distributions adopted in this work for the spins and magnetic fields.

Initial distribution	$B_{\rm birth}$ range (G)	$B_{\rm birth}$ distribution	$P_{\rm birth}$ range (ms)	$P_{\rm birth}$ distribution
U	$(10^{10}-10^{13})$	Uniform	$(10-100)$	Uniform
FL	$(10^{10}-10^{13})$	Flat in log	$(10-100)$	Uniform
FG	–	Faucher-Giguère & Kaspi (2006)	–	Faucher-Giguère & Kaspi (2006)

Table 3. Summary of the simulations. The initial distributions for spins and magnetic fields of NSs (U, FL, and FG) are summarized in Table 2. All models listed here have been run within the Empirical MW model. We have explored the same grid of parameters with the other MW models (EAGLE, ILLUSTRISTNG, and Const). All models assume the rapid-Gauss prescription for the SN explosion. Our fiducial model is highlighted in boldface in the Table.

	α	Init. Distr.	$\tau_{\rm d}$ (Gyr)		α	Init. Distr.	$\tau_{\rm d}$ (Gyr)
Ua0.5t0.1Emp	0.5	U	0.1	Ua3t0.1Emp	3	U	0.1
Ua0.5t0.5Emp	0.5	U	0.5	Ua3t0.5Emp	3	U	0.5
Ua0.5t1Emp	0.5	U	1	**Ua3t1Emp**	**3**	**U**	**1**
Ua0.5t2Emp	0.5	U	2	Ua3t2Emp	3	U	2
FLa0.5t0.1Emp	0.5	FL	0.1	FLa3t0.1Emp	3	FL	0.1
FLa0.5t0.5Emp	0.5	FL	0.5	FLa3t0.5Emp	3	FL	0.5
FLa0.5t1Emp	0.5	FL	1	FLa3t1Emp	3	FL	1
FLa0.5t2Emp	0.5	FL	2	FLa3t2Emp	3	FL	2
FGa0.5t0.1Emp	0.5	FG	0.1	FGa3t0.1Emp	3	FG	0.1
FGa0.5t0.5Emp	0.5	FG	0.5	FGa3t0.5Emp	3	FG	0.5
FGa0.5t1Emp	0.5	FG	1	FGa3t1Emp	3	FG	1
FGa0.5t2Emp	0.5	FG	2	FGa3t2Emp	3	FG	2
Ua1t0.1Emp	1	U	0.1	Ua5t0.1Emp	5	U	0.1
Ua1t0.5Emp	1	U	0.5	Ua5t0.5Emp	5	U	0.5
Ua1t1Emp	1	U	1	Ua5t1Emp	5	U	1
Ua1t2Emp	1	U	2	Ua5t2Emp	5	U	2
FLa1t0.1Emp	1	FL	0.1	FLa5t0.1Emp	5	FL	0.1
FLa1t0.5Emp	1	FL	0.5	FLa5t0.5Emp	5	FL	0.5
FLa1t1Emp	1	FL	1	FLa5t1Emp	5	FL	1
FLa1t2Emp	1	FL	2	FLa5t2Emp	5	FL	2
FGa1t0.1Emp	1	FG	0.1	FGa5t0.1Emp	5	FG	0.1
FGa1t0.5Emp	1	FG	0.5	FGa5t0.5Emp	5	FG	0.5
FGa1t1Emp	1	FG	1	FGa5t1Emp	5	FG	1
FGa1t2Emp	1	FG	2	FGa5t2Emp	5	FG	2

PSRPOPPY classifies a pulsar as dead if either it has crossed the death lines (equation 30) or if $\xi_R > \xi_{R,\max}$.

2.8.2 Beaming fraction

Pulsar radio emission is concentrated on collimated beams with finite width, so that pulsars sweep out only a limited area of the sky. As a consequence, we can detect only a fraction of the whole pulsar population, i.e. those whose beam crosses the observer's line of sight. The beaming fraction $f_{\rm beam}$ represents the fraction of pulsars beaming towards us. Previous studies agree that $f_{\rm beam}$ is period dependent. We adopt the prescription proposed in Tauris & Manchester (1998), an empirical relation obtained by fitting slow-rotating pulsars ($P \gtrsim 100$ ms),

$$f_{\rm beam} = 0.09\,(\log P - 1)^2 + 0.03 \qquad 0 \le f_{\rm beam} \le 1, \qquad (32)$$

where P is the spin period of the pulsar in seconds. Equation (32) shows that the beaming fraction is higher for pulsars spinning faster. Therefore such objects are also more likely to be detected. PSRPOPPY takes into account the beaming effects using a rejection sampling method: each pulsar can be detected with a probability $f_{\rm beam}$, computed according to equation (32).

2.8.3 Survey sensitivity

We use the radiometer equation (Dewey et al. 1985; Lorimer & Kramer 2004) to evaluate the minimum flux that a source must have to be detected

$$S_{\rm min} = \beta\, \frac{(S/N_{\rm min})\,(T_{\rm rec} + T_{\rm sky})}{G_A\,\sqrt{n_{\rm pol}\,t_{\rm int}\,\Delta\nu}} \sqrt{\frac{W}{P - W}}, \qquad (33)$$

where $S/N_{\rm min}$ is the minimum signal-to-noise ratio, β takes into account losses in sensitivity due to sampling antenna and digitalization noise, $n_{\rm pol}$ is the number of polarizations, $T_{\rm rec}$ and $T_{\rm sky}$ are the receiver and sky temperatures, G_A is the antenna gain, $\Delta\nu$ is the observing bandwidth, $t_{\rm int}$ is the integration time, W is the detected pulse width, and P is the pulse period. Most of the latter quantities are survey dependent (e.g. receiver temperature, observing bandwidth, integration time). PSRPOPPY evaluates the radiometer equation for the Parkes Multibeam Pulsar Survey (PMSURV; Manchester et al. 2001), the Swinburne Multibeam Pulsar Survey (SWINMB; Edwards et al. 2001), and the High Time Resolution Universe Pulsar Survey (HTRUP; Keith et al. 2010). For each survey, S/N$_{\rm min}$ is fixed to the value set by the survey itself. Moreover, the observed pulsars sample considered in our analyses includes only the objects detected by the surveys listed above. The effects caused by the propagation of the

pulsed signal through the interstellar medium enters equation (33) via W. In fact, collisions with free electrons cause a broadening of the received signal. Also, if $W \gtrsim P$ the signal is no longer detectable as the pulse is smeared into the background (Lorimer 2008, 2011).

PSRPOPPY assesses the observed pulse widths from the following relation (Burgay et al. 2003):

$$W^2 = W_i^2 + \tau_{samp}^2 + \left(\tau_{samp} \frac{DM}{DM_0} \right)^2 + \tau_{scatt}^2. \tag{34}$$

Here, W_i is the intrinsic pulse width, τ_{samp} is the sampling time-scale, τ_{scatt} is the mean scattering time-scale. DM and DM_0 are the dispersion measures in the direction of the pulsar and the diagonal dispersion of the survey, respectively. For simplicity, we fix the duty cycle $W_i/P = 0.05$ per cent for all pulsars (e.g. Lyne & Manchester 1988).

As the above quantities depend on the sky position of the source, we use the built-in functions of PSRPOPPY to plant our evolved pulsars in the Galaxy. PSRPOPPY employs the distribution obtained in Yusifov & Küçük (2004) to assign a radial position to each pulsar. Once assessed the position of the pulsar, the sky noise temperature T_{sky} is evaluated accordingly by fitting the Haslam et al. (1981) Table and rescaling for the correct frequency range (Szary et al. 2014). PSRPOPPY evaluates the dispersion measure DM by integrating the electron density n_e over the line of sight. For n_e we adopt the NE2001 model (Cordes 2004). Finally, DM is used to evaluate τ_{scatt} by applying the prescriptions described in Bhat et al. (2004).

The last missing ingredient is the luminosity. We adopt the luminosity function calculated in Faucher-Giguère & Kaspi (2006),

$$\log L = \log L_0 + \alpha_{F06} \log P + \beta_{F06} \log(\dot{P}/10^{-15}) + \delta_L, \tag{35}$$

with $L_0 = 0.18$ mJy kpc^2, δ_L is drawn from a normal distribution with $\sigma_{\delta_L} = 0.8$, $\alpha_{F06} = -1.5$ and $\beta_{F06} = 0.5$.

For each pulsar in the simulated Galactic population, we evaluate both S_{min} and the flux $F = L/(4\pi\mathcal{D}^2)$, where $\mathcal{D}$ is the pulsar distance. A source is detectable if $F > S_{min}$. We repeat this procedure for each survey, finally combining all the simulated-detected pulsars into a single sample.

2.8.4 Selection effects of binary systems

A comprehensive procedure to account for binary-pulsar selection effects is still unavailable. The Doppler shifting of the period causes a smearing of the signal and thus a reduction in the signal-to-noise ratio (Balakrishnan et al. 2022). This effect is stronger for binary systems with shorter periods and for shorter integration times. The Doppler shifting also depends on the eccentricity of the system. Bagchi, Lorimer & Wolfe (2013) show that the reduction in the signal-to-noise ratio decreases for higher eccentricity. Chattopadhyay et al. (2021) derive a fitting formula from the results of Bagchi et al. (2013). They assume an NS with a mass of 1.4 $M_\odot$, 1000 s duration of observation, and 60° inclination angle; then, fitting via linear regression for eccentricities $e = 0.1, 0.5$, and 0.8, they find a detection cut-off

$$P_{orb}/d \geq m \times P/s + c, \tag{36}$$

with

$$m = m_m e + c_m \tag{37}$$

$$c = m_c e + c_c, \tag{38}$$

where $m_m = -8.90$, $c_m = -27.68$, $m_c = -3.40$, and $c_c = 5.72$. Thus, pulsars in shorter orbital period binaries are also the most difficult to

be detected. We implement the aforementioned fit (Chattopadhyay et al. 2021) in PSRPOPPY.

2.8.5 Final set-up

Using the formalism discussed above we apply the radio selection effects on the final population of BNSs in the MW. We consider only the binaries survived in the MW until the present day and run PSRPOPPY on these catalogues. The code returns the sample of pulsars, picked from the initial catalogue, that are detectable by the selected surveys.

We ran PSRPOPPY multiple times on the total population, in order to filter out stochastic fluctuations. In this way, we obtain multiple realizations of the radio-selected pulsars. This procedure has a further advantage: as a bootstrap technique, it augments the statistic of our final sample.

We repeat this process for each of our models. For each simulation, we compare simulated and observed pulsars, according to three surveys (the Parkes Multibeam Pulsar Survey, Swinburne Multibeam Pulsar Survey, and High Time Resolution Universe Pulsar Survey, Section 2.8). We list the properties of the pulsars considered in this study in Table 4 (Manchester et al. 2005; Sengar et al. 2022).

2.9 Statistical analysis

We briefly summarize here the main points of the statistical framework used to compare the adopted models. In the following, we will denote the properties of the N_D observed pulsars (orbital period P_{orb}, eccentricity e, spin period P and rate of change of the spin period $\dot{P}$) with $D = \{P_{orb}, e, P, \dot{P}\}$, whereas θ_i denotes all the hyperparameters varied through the models (i.e. the SN explosion mechanism, the CE parameter α, the initial spin and magnetic-field distributions, the magnetic-field decay τ_d, and the MW model) and, by extension, the ith model itself.

To quantify the relative performance of two competing models in describing the available data, we will compute the Bayes' factor B_{12}[8]:

$$B_{12} = \frac{P(D, N_D|\theta_1)}{P(D, N_D|\theta_2)}. \tag{39}$$

In general, the likelihood $P(D|\theta)$ requires to evaluate the probability of the available data conditioned on the model. In this case, however, we do not have a functional relationship between the astrophysical hyperparameters θ and the pulsar's observed parameters.

On the other hand, we have catalogues of simulated observed pulsars, as described in Section 2.8. Each of these catalogues, denoted with $\xi(\theta)$, is composed of N_ξ pulsars, representative of the underlying observed distribution on the four pulsar properties. These realizations can be used to reconstruct this distribution and assign a probability for the data D.

The likelihood therefore becomes

$$P(D, N_D|\theta) = \int P(D, N_D|\xi(\theta), N_\xi) \, P(\xi(\theta), N_\xi|\theta) \, d\xi \, dN_\xi$$

$$= \int P(N_D|N_\xi) \, P(D|\xi(\theta)) \, P(\xi(\theta), N_\xi|\theta) \, d\xi \, dN_\xi. \tag{40}$$

---

[8]In general, to do model selection one should compute the odds ratio $O_{12} = B_{12} P(\theta_1)/P(\theta_2)$. However, under the assumption that the two models are a priori equally likely, the odds ratio reduces to the Bayes' factor.

Table 4. Sample of radio pulsars considered in this work. Column 1: pulsar name; column 2: spin P; column 3: spin derivative $\dot{P}$; column 4: magnetic field B; column 5: orbital period P_{orb}; column 6: eccentricity e; column 7: pulsar mass M_{psr}; column 8: companion mass M_{comp} (here we consider only pulsars which have another NS as companion); column 9: distance from the Sun; column 10: t_{GW} is the merging time of the binary systems, the BNSs with t_{GW} greater than the Hubble time (t_H) are shown with $>t_H$. The last column (column 12) shows in which surveys each pulsar has been discovered, the nomenclature is the same as in Section 2.8.

Radio pulsar	Type	P (ms)	$\dot{P}$ (10^{-18})	B $(10^9$ G)	P_{orb} (d)	e	M_{psr} $(M_\odot)$	M_{comp} $(M_\odot)$	Dist. (kpc)	t_{GW} (Myr)	Survey
J0737 − 3039 A[a]	recycled	22.7	1.76	2.0	0.102	0.088	1.338	1.249	1.15	86	PMSURV, HTRU
J0737 − 3039 B[a]	recycled	277.3	892.0	1590	0.102	0.088	1.249	1.338	1.15	86	PMSURV
J1325 − 6253[b]	recycled	28.9	0.048	1.2	1.815	0.064	<1.59	>0.98	4.4	$>t_H$	HTRU
J1753 − 2240[c]	recycled	95.1	0.970	2.7	13.638	0.304	–	–	3.46	$>t_H$	PMSURV, HTRU
J1755 − 2550[d]	young	315.2	2430	270	9.696	0.089	–	>0.40	10.3	$>t_H$	HTRU
J1756 − 2251[e]	recycled	28.5	1.02	1.7	0.320	0.181	1.341	1.230	0.73	1660	PMSURV, HTRU
J1757 − 1854[f]	recycled	21.5	2.63	7.6	0.184	0.606	1.338	1.395	7.40	78	HTRU
J1811 − 1736[g]	recycled	104.2	0.901	3.0	18.779	0.828	<1.64	>0.93	5.93	$>t_H$	PMSURV, HTRU
B1913 + 16[h]	recycled	59.0	8.63	7.0	0.323	0.617	1.440	1.389	9.80	301	PMSURV

References: [a]Kramer et al. (2006); Breton et al. (2008), [b]Sengar et al. (2022), [c]Keith et al. (2009), [d]Ng et al. (2015, 2018), [e]Faulkner et al. (2004), [f]Cameron et al. (2018), [g]Corongiu et al. (2007), [h]Hulse & Taylor (1975); Weisberg & Huang (2016).

The first term, $P(N_D|N_\xi)$, is an inhomogenous Poisson process:

$$P(N_D|N_\xi) = \frac{N_\xi^{N_D} e^{-N_\xi}}{N_D!}. \tag{41}$$

The probability $P(D|\xi(\theta))$ is modelled using a Dirichlet process Gaussian mixture model (DPGMM; e.g. Rinaldi & Del Pozzo 2022a, and references therein). The DPGMM can be used to approximate arbitrary probability densities given a set of samples drawn from the unknown distribution. In particular,

$$P(D|\xi(\theta)) = \int P(D|\lambda)\, P(\lambda|\xi(\theta))\, d\lambda\,, \tag{42}$$

where λ denotes the parameters of the DPGMM.

Both integrals can be calculated via Monte Carlo approximation, since we are able to sample $\xi(\theta)$ and N_ξ using the methods outlined above. Samples for λ, conditioned on a specific realization of $\xi(\theta)$, are drawn using FIGARO.[9]

With the Monte Carlo approximation, the full likelihood reads

$$P(D, N_D|\theta)$$
$$\simeq \frac{1}{M} \sum_{\xi_j(\theta)}^{\xi_M} \left(\frac{\left(N_{\xi_j}^{N_D} e^{-N_{\xi_j}}\right)/N_D!}{K} \sum_{\lambda_k|\xi_j(\theta)}^{\lambda_K} \prod_i P(D_i|\lambda_k) \right), \tag{43}$$

where K denotes the number of draws for λ and M the number of realizations for $\xi(\theta)$, and we made also use of the fact that the observations D are independent.

Using equation (43), we can compute the likelihood for each model and, consequently, discriminate between models. If $B_{12} > 1$, the model θ_1 is favoured over model θ_2. In the following, we will compute the Bayes' factor for each model over our fiducial 'Ua3t1Emp'.

3 RESULTS

3.1 Merger rates

Fig. 1 shows the BNS merger rate history for the Galaxy models and for the values of the CE parameter α adopted in this work. Table 5

[9]FIGARO is publicly available at https://github.com/sterinaldi/figaro.

Table 5. BNS merger rate in the MW at present time for different Galaxy models and values of the CE parameter α. All simulations shown in this figure assume $\tau_d = 1$ Gyr and the U distribution for initial spins and magnetic fields.

	Merger rates (Myr^{-1})			
		α		
MW model	0.5	1	3	5
EAGLE	2.2	12.6	20.5	12.9
ILLUSTRISTNG	2.7	16.3	24.5	16.2
Emp	3.6	21.5	31.3	17.7
Const	3.2	20.0	25.2	10.5

summarizes the BNS merger rates at present time predicted by our models. For comparison, we also show the BNS merger rate of the MW inferred by Pol et al. (2019, $\mathcal{R}_{MW} = 42^{+30}_{-14} \mathrm{Myr}^{-1}$) and Pol et al. (2020, $\mathcal{R}_{MW} = 37^{+24}_{-11} \mathrm{Myr}^{-1}$).

The parameter α has a large impact on the BNS merger rate. This result agrees with previous works, showing that almost all BNS mergers form via CE (Tauris et al. 2017; Giacobbo, Mapelli & Spera 2018; Kruckow et al. 2018; Mapelli & Giacobbo 2018; Vigna-Gómez et al. 2018; Mapelli et al. 2019; Mandel & Broekgaarden 2022; Iorio et al. 2023). In general, a larger value of α means that energy is transferred more efficiently to the envelope, facilitating its expulsion. In our models, the highest BNS merger rates are produced for $\alpha = 3$. Different values of α, both higher and lower, yield values of $\mathcal{R}_{MW}$ which are lower than the one inferred from observations by more than one standard deviation.

We find that the merger rate in the local Universe strongly correlates with the SFR of the Galaxy model (Artale et al. 2019). As such, the Galaxy models that better reproduce the observed $\mathcal{R}_{MW}$ are also the ones with the current SFR closer to the one of the MW. In particular, the Emp model with $\alpha = 3$ best reproduces the observed BNS merger rates (see Table 5). For this reason, we choose the Emp model as our fiducial model. In contrast, the EAGLE model underestimates the local BNS merger rate of the MW. In general, the merger rate history follows the same evolution with redshift as the SFR of the host galaxy, since most BNSs merge shortly after their formation. Our findings are in agreement with Artale et al. (2019),
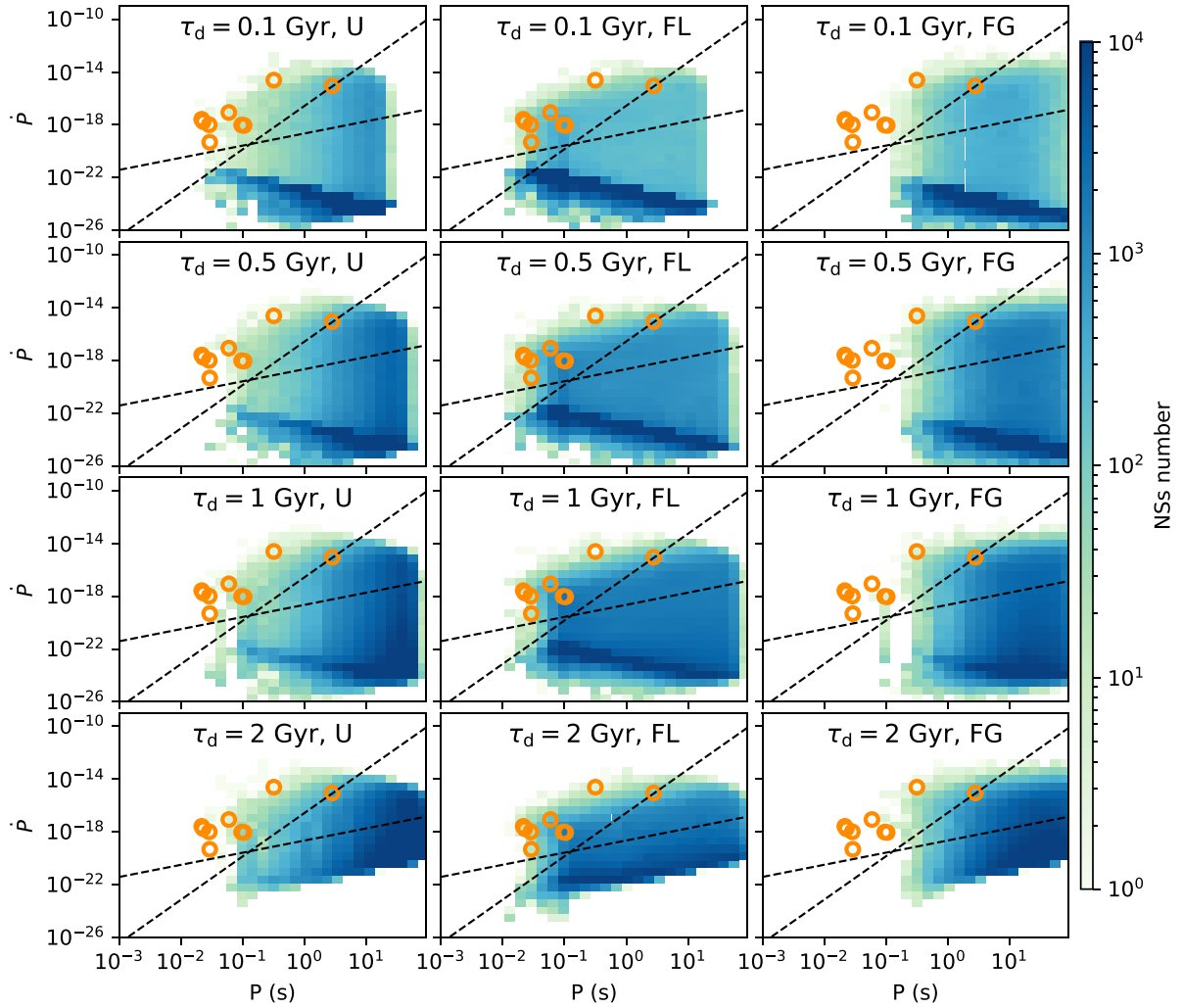
Figure 3. Distribution of the simulated BNSs at the present time in the P–$\dot{P}$ plane. Each column shows the results for a different model of the initial spin and magnetic field, from left to right: uniform (U), flat-in-log (FL), Faucher-Giguère (FG). The rows assume different values of τ_d, from top to bottom: $\tau_d = 0.1$, 0.5, 1, 2 Gyr. All the runs assume $\alpha = 3$ and the Emp MW model. The markers show the observed population of pulsars (Table 4). The dashed black lines show the death lines defined in equation (30).

who observe a tight correlation between the BNS merger rate and both the mass and the SFR of the host galaxy (see Artale et al. 2019; Artale et al. 2020a, b; Chattopadhyay et al. 2021, for more details on this correlation).

3.2 Orbital period–eccentricity

Fig. 2 shows the distributions of our simulated BNSs at look-back time $t_{lb} = 0$ (today) in the orbital period (P_{orb})– eccentricity (e) plane. We show the results varying α and the host Galaxy model. These plots do not include systems that have merged throughout the history of the MW, but only those that survived until today. All the simulations in Fig. 2 have $\tau_d = 1$ Gyr and an uniform (U) distribution for the initial spins and magnetic fields. Indeed, these parameters do not produce significant variations in the final distribution of the P_{orb}–e plane, as expected. The markers show the observed Galactic pulsars in BNS systems (Table 4).

Different models in Fig. 2 share similar trends. It is possible to distinguish a main branch characterized by short orbital periods (~ 1–10^3 d) and a second one, much less populated, with orbital

periods at $\sim 10^{5-6}$ d. At shorter periods, the distributions are bound by the GW merger time-scale ($t_{merge} \lesssim 1$ Myr).

The parameter α has a strong impact on the distribution of BNSs in the P_{orb}–e plane. In particular, the simulations with $\alpha = 5$ predict about twice as many BNSs as the $\alpha = 3$ model, and roughly five times more binaries compared to the $\alpha = 0.5$ model. This is expected as higher α values are associated with a more efficient expulsion of the CE, therefore more systems are able to survive the CE phase. In contrast, as we decrease α, the probability that a system prematurely merges during the CE increases (Iorio et al. 2023). These plots display another interesting feature: low-α simulations ($\alpha = 0.5$, 1) lack BNSs with low eccentricity, which are instead present in the $\alpha = 3$ and 5 models, favouring more eccentric binaries.

The host Galaxy model also plays a role on the final BNS distribution. In particular, we find that the most important parameter in this case is the total stellar mass $M_\star$ of the mock Galaxy. The procedure we adopt to populate a galaxy implies a direct correlation between $M_\star$ and the number of BNSs (see equation 24). For this reason the Const MW model produces a much lower number of final BNS systems.
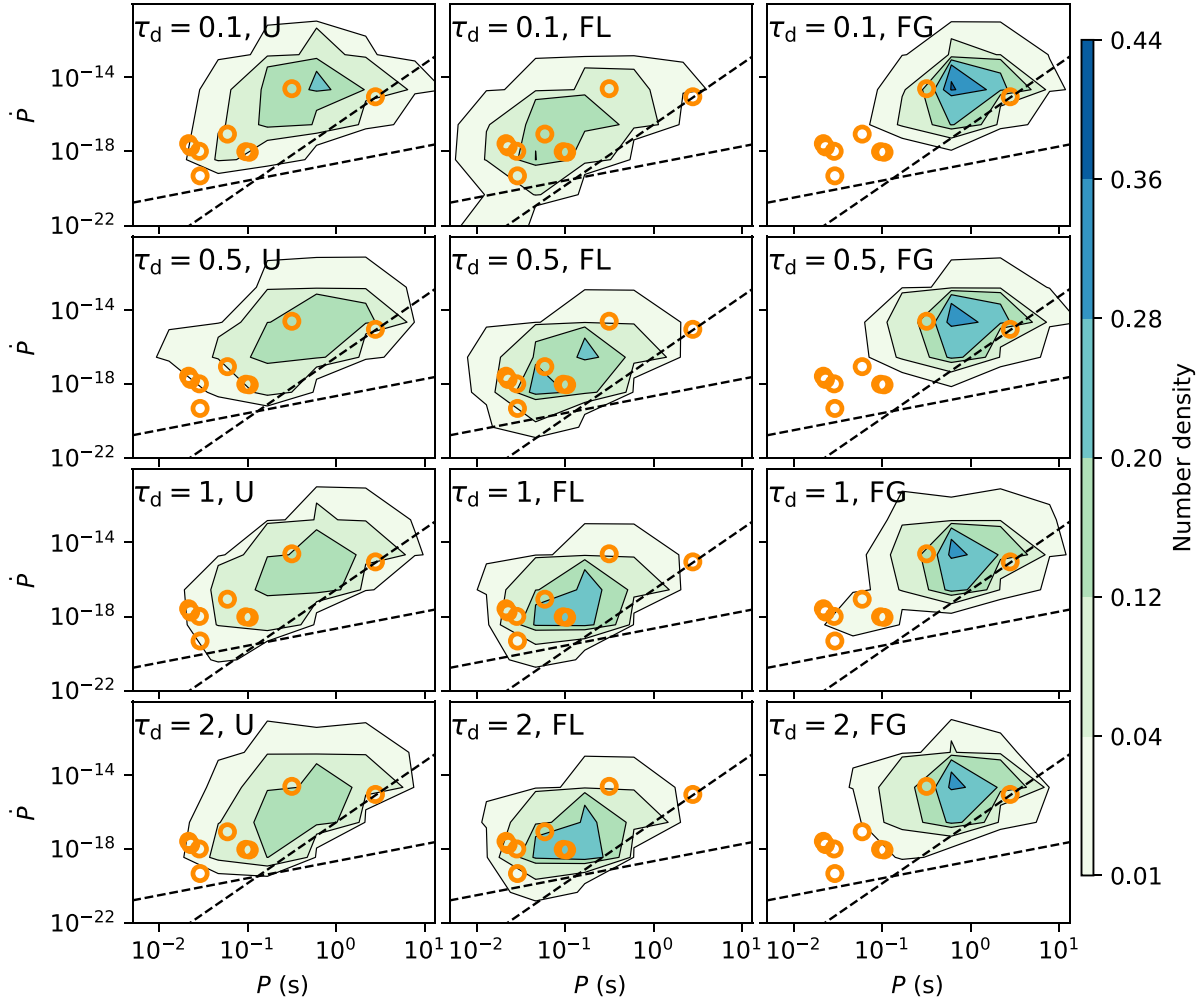
Figure 4. Isocontours showing the number density of detectable pulsars (after applying radio selection effects) in the $P - \dot{P}$ plane. Each column shows the results for a different spin and magnetic field model, from left to right: U, FL, and FG. The rows assume different values of τ_d, from top to bottom: $\tau_d = 0.1$, 0.5, 1, and 2 Gyr. All the runs assume $\alpha = 3$ and the Emp model for the MW. The markers show the observed population of pulsars (Table 4). The dashed black lines show the death lines defined in equation (30). The FG model can hardly account for the pulsars with the shortest periods and lowest values of $\dot{P}$, while models U and FL qualitatively match the location of the observed BNSs in the P–$\dot{P}$ plane.

Our results qualitatively agree with the observed BNS distribution of orbital periods and eccentricities. A more quantitative comparison is not straightforward owing to observational biases. In fact, eccentric binaries are more difficult to detect (Tauris et al. 2017), having stronger Doppler effects (Chattopadhyay et al. 2021).

3.3 P–$\dot{P}$ plane

Fig. 3 shows the distribution of our simulated BNSs at the present time in the P–$\dot{P}$ plane. We show the results varying τ_d and the model for the initial spins and magnetic fields. Fig. 3 clearly shows the importance of the initial spin and magnetic field distribution on the final pulsar population. Although the number of pulsars in each model varies with α and with the MW model, the shape of the distribution in the P–$\dot{P}$ plane is not significantly affected. Most of the detected BNSs in the MW data are characterized by a spin period $\lesssim 100$ ms. Most of the pulsars in the data set are probably recycled (Tauris et al. 2017). The primary-born pulsars in our models do not show striking differences compared to the second-born pulsars.

3.4 Selection effects

Fig. 3 shows the intrinsic astrophysical population, without accounting for radio selection effects. In contrast, Fig. 4 shows the distribution in the P–$\dot{P}$ plane of the detectable pulsars predicted by our models, obtained as described in Section 2.8 and averaging over $N = 100$ realizations of radio-selected pulsar populations. Fig. 4 shows the iso-density contours for models varying τ_d and the initial distributions of spins and magnetic fields (U, FL, and FG). The shapes of the contours depend on the chosen initial spins and magnetic fields: the pulsar density peak shifts in the parameter space because of these two parameters. The FG distribution generally produces slower spinning pulsars, with larger values of the spin periods P. In contrast, the FL distribution models peak at $P \sim 0.1$ s, where the majority of the observed pulsars lies. The U distribution, our fiducial model, shows a broader profile spanning a wider range of spin periods with respect to the other models.

We also calculate the number of pulsars predicted by our models. Our approach is completely self-consistent: we consider the specifics of the chosen surveys to account for radio selection effects, and
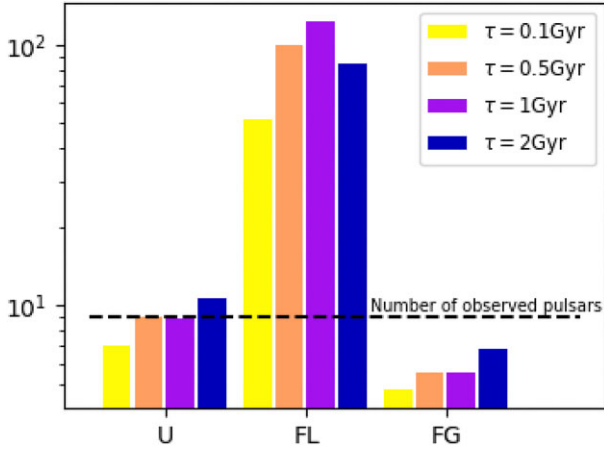
Figure 5. Mean number of radio-selected pulsars predicted by our models after averaging over the $N = 100$ realizations of the selection effects, assuming the fiducial $\alpha = 3$ and the Emp MW model. Each bar is a different model: the x-axis shows the spin and magnetic field initial distributions (U, FL, and FG). Each colour is associated with a different τ_d value: yellow, pink, purple, and blue for $\tau_d = 0.1, 0.5, 1,$ and 2 Gyr, respectively. The black horizontal dashed line shows the number of observed Galactic BNSs in the considered surveys, $N_{obs} = 9$. The FG (FL) model underestimates (overestimates) the number of observed pulsars, while the U model predicts a number of detectable BNSs which is very close to the observed value.

compare our samples with the pulsars observed by the same surveys. Fig. 5 shows the mean number of predicted detections averaged over the N realizations of the radio selection effects. The FL model seems to better fit the observed pulsar distribution in the P–$\dot{P}$ plane: the predicted pulsar sample peaks at ~ 0.1 s, where the majority of pulsars lie. However, Fig. 5 shows that the FL model predicts too many observed BNSs. In fact, it estimates $\sim 10^2$ observable pulsar binary systems, almost 10 times more than the number of detected Galactic BNSs. On the other hand, the FG model strongly underestimates the number of observed pulsars. The U model, instead, not only populates the P–$\dot{P}$ region where the observed pulsars lie, but also predicts the correct number of BNSs. For this reason, we choose the U model as the fiducial one. The reason why the FL model predicts a much higher number of detectable BNSs with respect to both FG and U is that it initializes the bulk of the pulsar population with lower values of both magnetic field and initial spin. Hence, more pulsars are still above the death line at current time in model FL compared to U and FG (Chattopadhyay et al. 2020).

From Figs 4 and 5, we can see another feature: the samples of detectable BNSs decrease for lower values of τ_d. This happens because younger pulsars constitute the great majority of the detectable pulsars. Since for lower values of τ_d the pulsars move faster in the P–$\dot{P}$ plane, towards larger spin periods and lower magnetic fields, pulsars cross the death line in shorter intervals of time.

Chattopadhyay et al. (2020) produce, in general, more radio selected pulsars with respect to our models, from 5 to 20 times more pulsars than our predictions (excluding their model CE–Z, which assumes no accretion during CE, as in our work, see Section 4). None the less, they observe the same trend with τ_d.

Fig. 6 shows the cumulative distributions of the orbital period, eccentricity, spin period, and spin period derivative, for our fiducial model. We show the distributions we obtained with and without accounting for the selection effects, for comparison. Radio selection effects select only the non-dead pulsars, characterized in general by smaller spin periods P and larger $\dot{P}$. Furthermore, binary
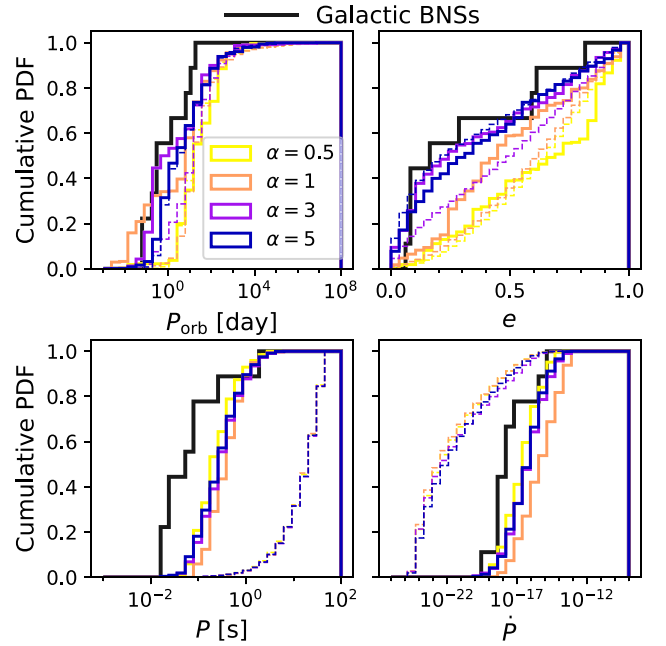
Figure 6. Cumulative distribution of the pulsar parameters P_{orb}, e, P, and $\dot{P}$ (from top left to bottom right) for the fiducial model parameters. Yellow, pink, purple, and blue solid lines: $\alpha = 0.5, 1, 5$. The dashed thin lines display the underlying astrophysical BNS population, while the solid thick lines show the detectable population, after implementing radio-selection effects. The black solid line marks the cumulative distribution of the observed Galactic BNSs. To account for radio-selection effects is crucial, especially in order to match the observed P–$\dot{P}$ distribution. We also note the good match between observed and simulated orbital eccentricity distribution after accounting for radio-selection effects.

selection effects tend to select circular with respect to eccentric systems.

In general, our models match the observed distributions, including the eccentricity distribution, when we account for selection effects.

Fig. 6 also compares different CE parameters $\alpha = 0.5-5$. The choice of α influences the orbital period and especially the eccentricity. The models with $\alpha > 1$ better match the data with respect to those with $\alpha \leq 1$, because the latter produce too many highly eccentric systems. This preference for $\alpha > 1$ when considering the eccentricity distribution points in the same direction as the result of the BNS merger rate: we found the best match with the MW merger rate for $\alpha = 3$.

The distributions of P and $\dot{P}$ do not change much with α, as expected. The Galactic BNSs seem to have a double peaked distribution: the first peak around $P \sim 1$ d, the second one at about 10^2 d (Andrews & Mandel 2019). However, given the small sample of detected BNSs we do not have enough statistics to claim that such feature is characteristic of the underlying BNS distribution.

3.5 Bayes factors

Table 6 shows the Bayes factors of each model that we obtained as described in Section 2.9. For this analysis, we used four BNS parameters: orbital period, eccentricity, spin period, and derivative of the spin period. Figs 7(a) and (b) show two examples of the DPGMMs we applied to these four parameters in our simulations.

The Bayes factors indicate that the FG distribution is strongly disfavoured in all the models, confirming what we can qualitatively

Table 6. Logarithmic Bayes factors (ln *B*) of the simulated models compared to the fiducial model 'Ua3t1Emp', adopting the Emp MW model. The fiducial model is highlighted in bold face in the table. The FL and FG prescriptions are disfavoured compared to the U model. Due to the low statistics of the observed pulsars sample, we cannot confidently choose a particular model based only on the Bayes factors.

	Uniform (U) τ_d (Gyr)				Flat in log (FL) τ_d (Gyr)				Faucher-Giguere (FG) τ_d (Gyr)			
α	0.1	0.5	1	2	0.1	0.5	1	2	0.1	0.5	1	2
0.5	−174 (195)	−98 (123)	−167(215)	−67(82)	−4 (37)	−18 (35)	−26 (32)	−35 (33)	−188 (177)	−216 (221)	−241 (261)	−38 (33)
1	−132 (181)	−91 (107)	−90 (124)	−71(112)	−4 (33)	−15 (31)	−29 (31)	−40 (31)	−156 (166)	−125 (157)	−124 (154)	−42 (32)
3	−12 (43)	0.9 (35)	**0 (37)**	0.3 (35)	−11 (28)	−55 (29)	−77 (30)	−45 (30)	−49 (76)	−29 (47)	−30 (58)	−23 (48)
5	1 (34)	−61 (97)	7 (31)	−27 (52)	−18 (28)	−75 (29)	−112 (30)	−163 (30)	−41 (106)	−37 (80)	−24 (53)	−37 (57)

see from Figs 4 and 5. Also, the U model performs better than the FL model, because the latter produces too many detectable BNSs (Fig. 5).

We find that the model with fiducial parameters, but assuming $\tau_d = 0.5$ Gyr (Ua3t0.5Emp), produces slightly better results. However, the differences yielded by distinct τ_d values are not as appreciable as those produced by different initial spin and magnetic field distributions. Thus, we cannot confidently discard a particular value of τ_d based only on this result.

3.6 Predictions for the SKA

Within our framework, we can make predictions for the Square Kilometre Array (SKA). We applied the radio selection effects setting the parameters of the major SKA surveys (MID and LOW, see Appendix C), and studied how the predictions vary for our different models. Table 7 shows the resulting number of SKA-detectable BNSs for different models. We see a spread of about two orders of magnitude among the results. Consistently with Fig. 5, the FL initial distribution predicts ∼10 times more observable pulsars than the other models. Our fiducial model estimates that SKA will be able to observe 30 ± 6 BNSs, among which 21 ± 4 new detections.

4 DISCUSSION

We have explored the BNS population properties within four different Galaxy models: a model with constant (Const) SFR, an empirical (Emp) MW model with exponentially decaying SFR, and two models taken from the EAGLE and ILLUSTRISTNG cosmological simulations, respectively (Table 1). In all the four models, the Galactic SFR at present-day matches the one of the MW. In addition, the Emp, EAGLE, and ILLUSTRISTNG models also match the current total stellar mass of the MW, whereas the Const model results in a factor of ∼2.5 lower mass Galaxy. Furthermore, the SFR history of the EAGLE and ILLUSTRISTNG galaxies deviate from the simple exponential decay assumed in the Emp model. The adopted models differ from each other in terms of metallicity as well: adopting the FMR, the Emp model is dominated by Solar metallicity stars, whereas the EAGLE and ILLUSTRISTNG models contain a large population of metal-poor stars.

Despite these differences, the $P_{orb}-e$ distribution of BNSs in the Emp, EAGLE, and ILLUSTRISTNG models show similar features. In contrast, the Const model predicts a much lower number of BNSs than the other models. This is a consequence of the lower total stellar mass of the Const model.

The Galactic BNS merger rate is primarily affected by our choice of the common-envelope parameter α. If we assume $\alpha = 3$, the resulting present-day Galactic merger rate is a factor of ∼10 higher than for $\alpha = 0.5$, and is more consistent with the value inferred from

observations (Pol et al. 2019, 2020). The merger rate is also affected by the SFR and metallicity of the adopted Galaxy model (Fig. 1).

Our models still represent a rather simplified description of the MW. Matteucci et al. (2019) and Kobayashi et al. (2023) explore detailed models of the MW, accounting also for its chemical enrichment history. They account for BNS mergers, and study if the latter can explain the *r*-process element abundance. Kobayashi et al. (2023) explain the relative abundances of elements through BNS mergers only with a dependence of the delay time distribution on metallicity, with lower metallicities yielding shorter delay times. Their comprehensive treatment goes beyond the purpose of this work.

Our models reproduce the orbital period and eccentricity distribution of Galactic BNSs, and match the observed BNS merger rate, in a self-consistent fashion. In particular, our fiducial model reproduces the double peak in the eccentricity distribution (Andrews & Mandel 2019): observed pulsars cluster around $e \sim 0.1$ and $e \sim 0.6$, showing instead a gap for $0.3 \lesssim e \lesssim 0.6$. In Fig. 2 ($\alpha = 3$), we can distinguish two more concentrated regions at eccentricity $e \sim 0.6$ and 0.1. This feature becomes even more evident after the application of radio selection effects (Fig. 7a). This suggests the importance of observational biases not only for the spins and magnetic fields of pulsars, but also for the orbital properties. Moreover, the distribution of pulsars in the $P_{orb}-e$ plane is almost independent of the chosen MW model, enforcing the robustness of this result.

We can compare our cumulative distributions (solid lines in Fig. 6) with the green dashed lines of Fig. 6 by Chattopadhyay et al. (2020). Our cumulative distribution of eccentricity is very different from the one reported by Chattopadhyay et al. (2020) because they do not account for binary selection effects. Our Fig. 2 can be compared with those of Vigna-Gómez et al. (2018) and Kruckow et al. (2018). The distribution of BNSs in fig. 11 of Kruckow et al. (2018) is less populated at high eccentricity with respect to our results. This difference is a consequence of the different kicks and binding energy prescriptions, as discussed in Iorio et al. (2023). Compared to Kruckow et al. (2018) and our results, Vigna-Gómez et al. (2018) produce much tighter binaries (coloured dots of their Fig. 2). In fact, most of the BNSs show orbital periods shorter than ∼10 d. Moreover, the wider systems ($P_{orb} \gtrsim 10^3$ d) are completely missing. This difference is a consequence of the different natal kick models adopted in Vigna-Gómez et al. (2018).

In our models, we did not include any spin-up prescription during the CE phase. In contrast, Chattopadhyay et al. (2020) assume that a NS accretes between 0.04 and 0.1 $M_\odot$ during CE, according to the rates presented in MacLeod & Ramirez-Ruiz (2015). As a result, pulsars spin up much more efficiently during a CE event than during RLO, and their distribution peaks toward smaller spin periods. For this reason, Chattopadhyay et al. (2020) predict many more detectable pulsars compared to our models when they enable accretion during CE. Nevertheless, the role played by the CE phase

(a)

(b)
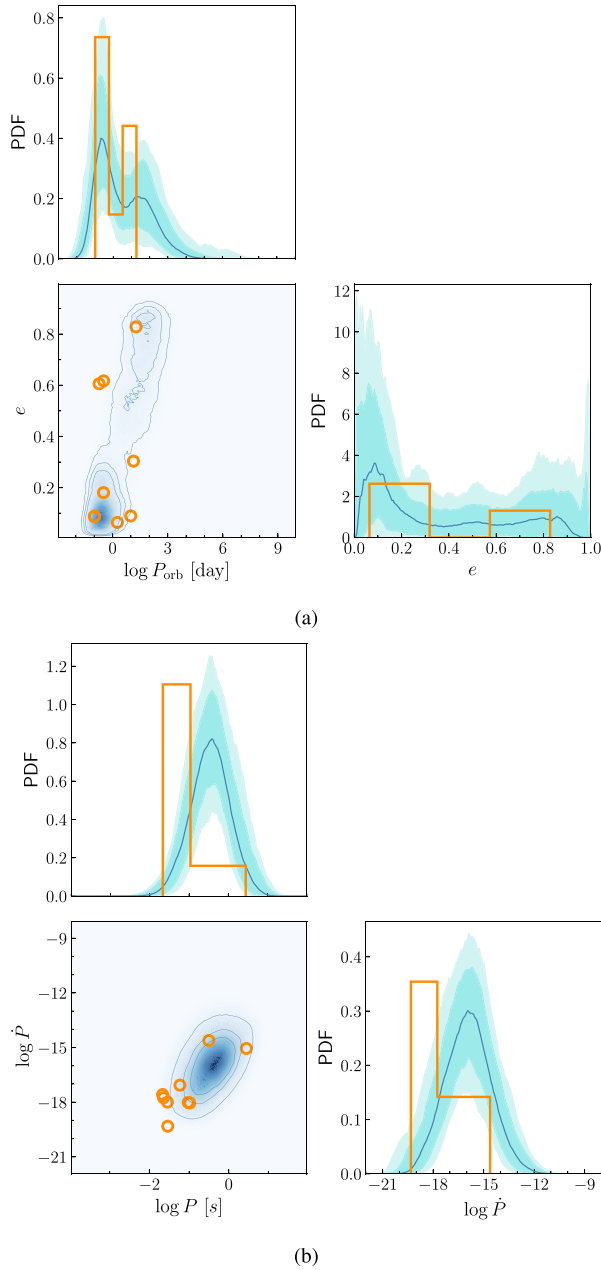
Figure 7. Two-dimensional likelihood for P_{orb} and e (panel a) and P and $\dot{P}$ (panel b) averaged over the simulated pulsars catalogues of our fiducial model (Ua3t1Emp), as reconstructed by FIGARO. These likelihoods are obtained by marginalizing out P and $\dot{P}$ or P_{orb} and e from the four-dimensional likelihood, respectively. The red circles and histograms show the observed Galactic BNSs (Table 4). The blue contour lines in the 2D plot show the 90 per cent, 68 per cent, and 50 per cent credible regions of the median distribution (blue lines in 1D plots). The shaded regions in 1D plots represent the 68 per cent and 90 per cent credible intervals for the marginal probability density for each parameter.

during spin-up is controversial (Chamandy et al. 2018). Osłowski et al. (2011) assume that the accreted matter during CE contributes only to the magnetic field decay, considering accretion during CE a chaotic process, not able to produce spin-up (Benensohn, Lamb & Taam 1997). Our spin-up treatment does not include the effect of winds as well. Indeed, we might expect the infalling matter produced by winds to be chaotic and thus not efficiently cause

the spin-up of the pulsar (Kiel et al. 2008). We can compare Fig. 5 with table 4 from Chattopadhyay et al. (2020). The number of detectable pulsars predicted by their models is generally one order of magnitude higher than our predictions. Our predicted numbers of observable pulsars are consistent only with their model CE–Z, which does not include spin-up during CE, and predicts 13 observations.

There are large uncertainties about the surface magnetic field: the burial of magnetic field during mass accretion is poorly understood as well as its decay during the isolated pulsar evolution. The τ_d parameter has been varied in the literature from a few Myr (e.g. Osłowski et al. 2011) up to a few Gyr (e.g. Kiel et al. 2008). Another important contribution to the overall uncertainty in the pulsar population is given by the initial distribution of spins and magnetic fields. These are even more important than the magnetic-field decay time τ_d. Several distributions have been proposed for the initial spin and magnetic field (e.g. Faucher-Giguère & Kaspi 2006; Igoshev et al. 2022). However, the lack of statistics does not allow us to draw strong conclusions.

We evaluated a four-dimensional likelihood in the (P_{orb}, e, P, $\dot{P}$) space. Our approach consistently takes into account correlations among parameters, which are instead neglected by other tests (e.g. the Kolmogorov-Smirnov test), frequently used in the pulsar literature. The large errors on the Bayes factor errors reported in Table 6 are a consequence of the limited number of observed pulsars, making it difficult to differentiate among the models. However, despite this limitation, the Bayes factor indicate that the FG and FL models are disfavoured with respect to the U prescription.

We can compare our SKA predictions (Table 7) to table 4 of Chattopadhyay et al. (2021). Their fiducial model estimates 78 BNSs containing a radio-detectable pulsar by the SKA telescope. Their result is thus roughly twice our projection. Nevertheless this discrepancy is consistent with the different approach we used. As already stressed, the different CE formalism, accentuates the spin up of their pulsars, resulting in shorter spin periods. In turn, this translates into a higher number of detectable pulsars.

5 SUMMARY AND CONCLUSIONS

The BNS population of the MW is the perfect laboratory to test binary-star evolution models. Here, we used the new population synthesis code SEVN (Iorio et al. 2023) to model the population of BNSs in the MW. We implemented a new model for both the spin down and spin up of pulsars in SEVN, while also probing the relevant parameter space (e.g. CE parameter α, initial spin distribution, initial magnetic field distribution, decay time of the magnetic field τ_d). We injected our simulated binaries into four MW models: an empirical model with an exponentially decaying SFR, a model with constant SFR, and two galaxies from the EAGLE and ILLUSTRISTNG cosmological simulations.

We compared our simulated BNS catalogues with the observed Galactic BNSs after applying radio selection effects with PSRPOPPY (Bates et al. 2014). In our analysis, we considered four observable parameters: orbital period, eccentricity, pulsar spin period, and spin period derivative. After modelling our radio-selected pulsars with a Dirichlet process Gaussian mixture model (Rinaldi & Del Pozzo 2022b), we evaluated the four-dimensional likelihood associated with each model in the aforementioned parameter space. We then compared our models by computing the Bayes factor with respect to the fiducial model.

We also derived the Galactic BNS merger rate from our models and compared it with the one inferred from the observations (Pol

Table 7. Predicted number of pulsars in BNSs detectable by the SKA, after averaging over $N = 100$ realizations of the radio selection effects. We report the standard deviation on the mean within brackets. The fiducial model is highlighted in bold face in the table.

	Uniform (U) τ_d (Gyr)				Flat in log (FL) τ_d (Gyr)				Faucher-Giguere (FG) τ_d (Gyr)			
α	0.1	0.5	1	2	0.1	0.5	1	2	0.1	0.5	1	2
0.5	6 (2)	10 (3)	9 (3)	11 (3)	54 (8)	121 (10)	173 (12)	211 (14)	3 (1)	5 (2)	4 (2)	210 (14)
1	9 (3)	13 (3)	10 (3)	14 (3)	84 (8)	145 (13)	196 (12)	241 (13)	6 (2)	6 (2)	7 (3)	240 (14)
3	23 (5)	29 (5)	**30(6)**	36 (5)	155 (12)	316 (19)	411 (18)	288 (17)	17 (4)	21 (4)	20 (4)	22 (5)
5	26 (5)	16 (4)	39 (6)	21 (5)	178 (14)	395 (20)	532 (24)	721 (29)	17 (4)	19 (4)	23 (5)	21 (5)

et al. 2019, 2020). The CE parameter α has a large impact on both the merger rate and the orbital properties of the BNS population. The present-day BNS merger rate varies up to one order of magnitude depending on the choice of α. Values of $\alpha < 1$ are disfavoured, as they underpredict the merger rates and produce more eccentric systems compared to observations (Fig. 6). Assuming the empirical MW prescription, the model with $\alpha = 3$ produces a rate $\mathcal{R}_{MW} = 31.3$ Myr^{-1} (Fig. 1), consistent with the rate inferred from the Galactic pulsar binary systems ($\mathcal{R}_{MW} = 37^{+24}_{-11}$ Myr^{-1}, Pol et al. 2020).

The distribution of magnetic field and spin period at pulsar formation play a critical role on the final population of detectable pulsars (Fig. 4). The Bayes factors favour the uniform (U) distribution of spin periods and magnetic fields, which predicts 5–10 detectable pulsars. In contrast, the flat-in-log (FL) model predicts ∼100 detectable pulsars (Fig. 5) against the 9 observed Galactic pulsars in the considered surveys (the Parkes Multibeam Pulsar Survey, the Swinburne Multibeam Pulsar Survey, and the High Time Resolution Universe Pulsar Survey).

The magnetic field decay time-scale τ_d is another free parameter of our model. There are large uncertainties on the physical process leading to the burial of the magnetic field and consequently to the typical time-scales associated with it. τ_d dictates the speed at which a pulsar traverses the P–$\dot{P}$ plane and stops emitting radio beams. Given the small sample of Galactic BNSs, we cannot draw strong conclusions on the expected τ_d value.

We have shown that we need to account for radio selection effects in order to reproduce the observed spin period and magnetic field distributions of observed pulsars. Moreover, binary selection effects are critical to correctly match the orbital period and especially the eccentricity distribution of the observed Galactic BNSs.

According to our fiducial model, which matches both the Galactic merger rate and the orbital properties of Galactic BNSs, the SKA will observe ∼30 BNSs in the MW, among which ∼20 new detections.

Our results show that we can match the BNS merger rate, as inferred from Galactic radio pulsars, only if we assume an empirical MW model, a value of the CE parameter $\alpha \approx 3$, and the natal kick model by Giacobbo & Mapelli (2020). Such model yields low natal kicks for stripped and ultra-stripped SNe in binary systems. The Galactic BNS merger rate drops by a factor of 4 for larger natal kicks (Hobbs et al. 2005). This result favours low natal kicks in tight binary systems, as already suggested by previous studies (e.g. Beniamini & Piran 2016; Bray & Eldridge 2016, 2018; Mapelli & Giacobbo 2018; Vigna-Gómez et al. 2018; Willcox et al. 2021; O'Doherty et al. 2023; Richards et al. 2023).

An accurate model for the star formation history of the MW is essential, in order to describe the current BNS merger rate and number of observable pulsars. The treatment of CE is also important but more prone to uncertainties about single star evolution and mass transfer. For example, Santoliquido et al. (2021), who adopt a different formalism for single star evolution, predict even larger merger rates for $\alpha > 3$, while the BNS merger rate estimated with SEVN has a peak for $\alpha = 3$ and then decreases for larger values of α (Iorio et al. 2023).

The magnetic field and spin model are essential to match both the number of observed pulsars in BNSs and their position in the P–$\dot{P}$ plane, the FG and FL models being less favoured compared to an uniform distribution for the initial magnetic field and spin period. However, a link between the initial magnetic field distribution and the underlying physical processes that govern the magnetic field evolution is still highly debated (Konar 2017; Igoshev et al. 2022; Zhang et al. 2022; Sarin, Brandenburg & Haskell 2023). Here, we have assumed that CE evolution does not contribute to pulsar spin up. This is a crucial assumption and needs further consideration with dedicated hydrodynamical numerical simulations.

DATA AVAILABILITY

This work made use of the codes SEVN (Iorio et al. 2023) available at the gitlab repository https://gitlab.com/sevncodes/sevn (release *Sgalletta23*, https://gitlab.com/sevncodes/sevn/-/releases/sgalletta23), and FIGARO, presented in Rinaldi & Del Pozzo (2022b). The list of SEVN parameters used in this work can be found at the following link: https://doi.org/10.5281/zenodo.7887279 (Sgalletta et al. 2023). Further data will be shared based on reasonable request to the corresponding authors.

REFERENCES

Abbott B. P. et al., 2017a, Phys. Rev. Lett., 119, 161101

Abbott B. P. et al., 2017b, ApJ, 848, L12

Abbott B. P. et al., 2018, Phys. Rev. Lett., 121, 161101

Abbott B. P. et al., 2020, ApJ, 892, L3

Ade P. A. R. et al., 2014, A&A, 571, A16

Ade P. A. R. et al., 2016, A&A, 594, A13

Andersen B. C., Ransom S. M., 2018, ApJ, 863, L13

Andrews J. J., Mandel I., 2019, ApJ, 880, L8

Artale M. C., Mapelli M., Giacobbo N., Sabha N. B., Spera M., Santoliquido F., Bressan A., 2019, MNRAS, 487, 1675

Artale M. C., Mapelli M., Bouffanais Y., Giacobbo N., Pasquato M., Spera M., 2020a, MNRAS, 491, 3419

Artale M. C., Bouffanais Y., Mapelli M., Giacobbo N., Sabha N. B., Santoliquido F., Pasquato M., Spera M., 2020b, MNRAS, 495, 1841

Arzoumanian Z. et al., 2018, ApJS, 235, 37

Arzoumanian Z. et al., 2020, ApJ, 905, L34

Asplund M., Grevesse N., Sauval A. J., Scott P., 2009, ARA&A, 47, 481

Atri P. et al., 2019, MNRAS, 489, 3116

Bagchi M., Lorimer D., Wolfe S., 2013, MNRAS, 432, 1303

Balakrishnan V., Champion D., Barr E., Kramer M., Venkatraman Krishnan V., Eatough R. P., Sengar R., Bailes M., 2022, MNRAS, 511, 1265

Bates S. D., Lorimer D. R., Rane A., Swiggum J., 2014, MNRAS, 439, 2893

Bauswein A., Just O., Janka H.-T., Stergioulas N., 2017, ApJ, 850, L34

Belczynski K. et al., 2018, A&A, 615, A91

Belczynski K. et al., 2020, A&A, 636, A104

Benensohn J. S., Lamb D. Q., Taam R. E., 1997, ApJ, 478, 723

Beniamini P., Piran T., 2016, MNRAS, 456, 4089

Beniamini P., Piran T., 2019, MNRAS, 487, 4847

Bhat N. D. R., Cordes J. M., Camilo F., Nice D. J., Lorimer D. R., 2004, ApJ, 605, 759

Bhattacharya D., Wijers R. A. M. J., Hartman J. W., Verbunt F., 1992, A&A, 254, 198

Blaauw A., 1961, Bull. Astron. Inst. Netherlands, 15, 265

Boco L., Lapi A., Goswami S., Perrotta F., Baccigalupi C., Danese L., 2019, ApJ, 881, 157

Boco L., Lapi A., Chruslinska M., Donevski D., Sicilia A., Danese L., 2021, ApJ, 907, 110

Bogdanov S., Heinke C. O., Özel F., Güver T., 2016, ApJ, 831, 184

Bouffanais Y., Mapelli M., Santoliquido F., Giacobbo N., Iorio G., Costa G., 2021, MNRAS, 505, 3873

Bovy J., 2017, MNRAS, 470, 1360

Bray J. C., Eldridge J. J., 2016, MNRAS, 461, 3747

Bray J. C., Eldridge J. J., 2018, MNRAS, 480, 5657

Bressan A., Marigo P., Girardi L., Salasnich B., Dal Cero C., Rubele S., Nanni A., 2012, MNRAS, 427, 127

Breton R. P. et al., 2008, Science, 321, 104

Broekgaarden F. S. et al., 2021, MNRAS, 508, 5028

Broekgaarden F. S. et al., 2022, MNRAS, 516, 5737

Brown G. E., 1995, ApJ, 440, 270

Burgay M. et al., 2003, Nature, 426, 531

Cameron A. D. et al., 2018, MNRAS, 475, L57

Chamandy L. et al., 2018, MNRAS, 480, 1898

Chattopadhyay D., Stevenson S., Hurley J. R., Rossi L. J., Flynn C., 2020, MNRAS, 494, 1587

Chattopadhyay D., Stevenson S., Hurley J. R., Bailes M., Broekgaarden F., 2021, MNRAS, 504, 3682

Chiappini C., Matteucci F., Gratton R., 1997, ApJ, 477, 765

Chruślińska M., Belczynski K., Klencki J., Benacquista M., 2018, MNRAS, 474, 2937

Chruślińska M., Nelemans G., Boco L., Lapi A., 2021, MNRAS, 508, 4994

Claeys J. S. W., Pols O. R., Izzard R. G., Vink J., Verbunt F. W. M., 2014, A&A, 563, A83

Coleman M. S. B., Burrows A., 2022, MNRAS, 517, 3938

Colombo A., Salafia O. S., Gabrielli F., Ghirlanda G., Giacomazzo B., Perego A., Colpi M., 2022, ApJ, 937, 79

Combi L., Siegel D. M., 2023, ApJ, 944, 28

Cordes J. M., 2004, in Clemens D., Shah R., Brainerd T., eds, ASP Conf. Ser. Vol. 317, Milky Way Surveys: The Structure and Evolution of our Galaxy. Astron. Soc. Pac., San Francisco, p. 211

Cordes J. M., Lazio T. J. W., 2002, preprint (arXiv:astro-ph/0207156)

Corongiu A., Kramer M., Stappers B. W., Lyne A. G., Jessner A., Possenti A., D'Amico N., Löhmer O., 2007, A&A, 462, 703

Costa G., Girardi L., Bressan A., Marigo P., Rodrigues T. S., Chen Y., Lanza A., Goudfrooij P., 2019, MNRAS, 485, 4641

Costa G., Bressan A., Mapelli M., Marigo P., Iorio G., Spera M., 2021, MNRAS, 501, 4514

Côté B. et al., 2019, ApJ, 875, 106

Courteau S. et al., 2014, Rev. Mod. Phys., 86, 47

Dewey R. J., Taylor J. H., Weisberg J. M., Stokes G. H., 1985, ApJ, 294, L25

Dewi J. D. M., Podsiadlowski P., Sena A., 2006, MNRAS, 368, 1742

Di Stefano R., Kruckow M. U., Gao Y., Neunteufel P. G., Kobayashi C., 2023, ApJ, 944, 87

Edwards R. T., Bailes M., van Straten W., Britton M. C., 2001, MNRAS, 326, 358

Eggleton P. P., 1983, ApJ, 268, 368

Eichler D., Livio M., Piran T., Schramm D. N., 1989, Nature, 340, 126

Faucher-Giguère C.-A., Kaspi V. M., 2006, ApJ, 643, 332

Faulkner A. J. et al., 2004, MNRAS, 355, 147

Fragos T., Andrews J. J., Ramirez-Ruiz E., Meynet G., Kalogera V., Taam R. E., Zezas A., 2019, ApJ, 883, L45

Fryer C. L., Belczynski K., Wiktorowicz G., Dominik M., Kalogera V., Holz D. E., 2012, ApJ, 749, 91

Fujibayashi S., Kiuchi K., Wanajo S., Kyutoku K., Sekiguchi Y., Shibata M., 2023, ApJ, 942, 39

Gessner A., Janka H.-T., 2018, ApJ, 865, 61

Giacobbo N., Mapelli M., 2018, MNRAS, 480, 2011

Giacobbo N., Mapelli M., 2019, MNRAS, 482, 2234

Giacobbo N., Mapelli M., 2020, ApJ, 891, 141

Giacobbo N., Mapelli M., Spera M., 2018, MNRAS, 474, 2959

Goldreich P., Julian W. H., 1969, ApJ, 157, 869

Goldreich P., Reisenegger A., 1992, ApJ, 395, 250

Goldstein A. et al., 2017, ApJ, 848, L14

Gonthier P. L., Van Guilder R., Harding A. K., 2004, ApJ, 604, 775

Grisoni V., Spitoni E., Matteucci F., Recio-Blanco A., de Laverny P., Hayden M., Mikolaitis Ŝ., Worley C. C., 2017, MNRAS, 472, 3637

Harris C. R. et al., 2020, Nature, 585, 357

Haslam C. G. T., Klein U., Salter C. J., Stoffel H., Wilson W. E., Cleary M. N., Cooke D. J., Thomasson P., 1981, A&A, 100, 209

Hewish A., Bell S. J., Pilkington J. D. H., Scott P. F., Collins R. A., 1968, Nature, 217, 709

Hirai R., Mandel I., 2022, ApJ, 937, L42

Hobbs G., 2013, Class. Quant. Gravity, 30, 224007

Hobbs G., Lorimer D. R., Lyne A. G., Kramer M., 2005, MNRAS, 360, 974

Hobbs G. et al., 2010, Class. Quant. Gravity, 27, 084013

Hotokezaka K., Beniamini P., Piran T., 2018, Int. J. Modern Phys. D, 27, 1842005

Hulse R. A., Taylor J. H., 1975, ApJ, 195, L51

Hunt L., Dayal P., Magrini L., Ferrara A., 2016, MNRAS, 463, 2020

Hunter J. D., 2007, Comput. Sci. Eng., 9, 90

Hurley J. R., Tout C. A., Pols O. R., 2002, MNRAS, 329, 897

Igoshev A. P., Frantsuzova A., Gourgouliatos K. N., Tsichli S., Konstantinou L., Popov S. B., 2022, MNRAS, 514, 4606

Illarionov A. F., Sunyaev R. A., 1975, A&A, 39, 185

Iorio G. et al., 2023, MNRAS, 524, 426

Ivanova N. et al., 2013, A&AR, 21, 59

Janka H. T., Mueller E., 1994, A&A, 290, 496

Justham S., Podsiadlowski P., Han Z., 2011, MNRAS, 410, 984

Kapil V., Mandel I., Berti E., Müller B., 2023, MNRAS, 519, 5893

Kasen D., Metzger B., Barnes J., Quataert E., Ramirez-Ruiz E., 2017, Nature, 551, 80

Kaspi V. M., Taylor J. H., Ryba M. F., 1994, ApJ, 428, 713

Keith M. J., Eatough R. P., Lyne A. G., Kramer M., Possenti A., Camilo F., Manchester R. N., 2009, MNRAS, 395, 837

Keith M. J. et al., 2010, MNRAS, 409, 619

Kiel P. D., Hurley J. R., Bailes M., Murray J. R., 2008, MNRAS, 388, 393
Klencki J., Nelemans G., Istrate A. G., Chruslinska M., 2021, A&A, 645, A54
Kobayashi C. et al., 2023, ApJ, 943, L12
Konar S., 2017, J. Astrophys. Astron., 38, 47
Konar S., Bhattacharya D., 1997, MNRAS, 284, 311
Konar S., Bhattacharya D., 1999, MNRAS, 303, 588
Kramer M. et al., 2006, Science, 314, 97
Kramer M. et al., 2021, Phys. Rev. X, 11, 041050
Kroupa P., 2001, MNRAS, 322, 231
Kruckow M. U., Tauris T. M., Langer N., Kramer M., Izzard R. G., 2018, MNRAS, 481, 1908
Lai D., Chernoff D. F., Cordes J. M., 2001, ApJ, 549, 1111
Lattimer J. M., 2021, Annu. Rev. Nucl. Part. Sci., 71, 433
Lentati L. et al., 2015, MNRAS, 453, 2576
Licquia T. C., Newman J. A., 2015, ApJ, 806, 96
Lipunov V. M., Postnov K. A., Prokhorov M. E., 1997, MNRAS, 288, 245
Lorimer D. R., 2008, Living Rev. Relativ., 11, 8
Lorimer D., 2011, Astrophysics Source Code Library, record ascl:1107.016
Lorimer D. R., Kramer M., 2004, Handbook of Pulsar Astronomy. Vol. 4, Cambridge Univ. Press, Cambridge
Lyne A. G., Manchester R. N., 1988, MNRAS, 234, 477
Lyne A. G. et al., 2004, Science, 303, 1153
Lyne A., Hobbs G., Kramer M., Stairs I., Stappers B., 2010, Science, 329, 408
MacLeod M., Ramirez-Ruiz E., 2015, ApJ, 803, 41
Manchester R. N. et al., 2001, MNRAS, 328, 17
Manchester R. N., Hobbs G. B., Teoh A., Hobbs M., 2005, AJ, 129, 1993
Manchester R. N. et al., 2013, PASA, 30, e017
Mandel I., Broekgaarden F. S., 2022, Living Rev. Relativ., 25, 1
Mannucci F., Cresci G., Maiolino R., Marconi A., Gnerucci A., 2010, MNRAS, 408, 2115
Mannucci F., Salvaterra R., Campisi M. A., 2011, MNRAS, 414, 1263
Mapelli M., Giacobbo N., 2018, MNRAS, 479, 4391
Mapelli M., Giacobbo N., Ripamonti E., Spera M., 2017, MNRAS, 472, 2422
Mapelli M., Giacobbo N., Santoliquido F., Artale M. C., 2019, MNRAS, 487, 2
Mapelli M., Spera M., Montanari E., Limongi M., Chieffi A., Giacobbo N., Bressan A., Bouffanais Y., 2020, ApJ, 888, 76
Martinez J. G. et al., 2015, ApJ, 812, 143
Matteucci F., Romano D., Cescutti G., Simonetti P., 2019, Rendiconti Lincei. Scienze Fisiche e Naturali, 30, 85
McMillan P. J., 2017, MNRAS, 465, 76
Metzger B. D., 2017, Living Rev. Relativ., 20, 3
Metzger B. D., 2019, Living Rev. Relativ., 23, 1
Miles M. T. et al., 2023, MNRAS, 519, 3976
Müller B. et al., 2019, MNRAS, 484, 3307
Murase K. et al., 2018, ApJ, 854, 60
Nedora V., Dietrich T., Shibata M., Pohl M., Crosato Menegazzi L., 2023, MNRAS, 520, 2727
Neijssel C. J. et al., 2019, MNRAS, 490, 3740
Nelemans G., Verbunt F., Yungelson L. R., Portegies Zwart S. F., 2000, A&A, 360, 1011
Nelson D. et al., 2019a, Comput. Astrophys. Cosmol., 6, 2
Nelson D. et al., 2019b, MNRAS, 490, 3234
Ng C. et al., 2015, MNRAS, 450, 2922
Ng C. et al., 2018, MNRAS, 476, 4315
Nguyen C. T. et al., 2022, A&A, 665, A126
Nordhaus J., Brandt T. D., Burrows A., Livne E., Ott C. D., 2010, Phys. Rev. D, 82, 103016
Nordhaus J., Brandt T. D., Burrows A., Almgren A., 2012, MNRAS, 423, 1805
O'Doherty T. N., Bahramian A., Miller-Jones J. C. A., Goodwin A. J., Mandel I., Willcox R., Atri P., Strader J., 2023, MNRAS, 521, 2504
Olejak A., Belczynski K., Ivanova N., 2021, A&A, 651, A100
Olejak A., Fryer C. L., Belczynski K., Baibhav V., 2022, MNRAS, 516, 2252
Osłowski S., Bulik T., Gondek-Rosińska D., Belczyński K., 2011, MNRAS, 413, 461

Ostriker J. P., Gunn J. E., 1969, ApJ, 157, 1395
Özel F., Psaltis D., Narayan R., Santos Villarreal A., 2012, ApJ, 757, 55
Özel F., Psaltis D., Güver T., Baym G., Heinke C., Guillot S., 2016, ApJ, 820, 28
Pacini F., 1968, Nature, 219, 145
Paczynski B., 1976, in Eggleton P., Mitton S., Whelan J., eds, Proc. IAU Symp. Vol. 73, Structure and Evolution of Close Binary Systems. Kluwer, Dordrecht, p. 75
Perna R., Artale M. C., Wang Y.-H., Mapelli M., Lazzati D., Sgalletta C., Santoliquido F., 2022, MNRAS, 512, 2654
Peters P. C., 1964, Phys. Rev., 136, B1224
Pezzulli G., Fraternali F., 2015, MNRAS, 455, 2308
Pillepich A. et al., 2019, MNRAS, 490, 3196
Pillepich A. et al., 2023, preprint (arXiv:2303.16217)
Pol N., McLaughlin M., Lorimer D. R., 2019, ApJ, 870, 71
Pol N., McLaughlin M., Lorimer D. R., 2020, Res. Notes Am. Astron. Soc., 4, 22
Portegies Zwart S. F., Yungelson L. R., 1998, A&A, 332, 173
Radice D., Bernuzzi S., Perego A., 2020, Annu. Rev. Nucl. Part. Sci., 70, 95
Richards S. M., Eldridge J. J., Briel M. M., Stevance H. F., Willcox R., 2023, MNRAS, 522, 3972
Riley J. et al., 2022, ApJS, 258, 34
Rinaldi S., Del Pozzo W., 2022a, MNRAS, 509, 5454
Rinaldi S., Del Pozzo W., 2022b, MNRAS, 517, L5
Röpke F. K., De Marco O., 2023, Living Rev. Comput. Astrophys., 9, 2
Rudak B., Ritter H., 1994, MNRAS, 267, 513
Sana H. et al., 2012, Science, 337, 444
Santoliquido F., Mapelli M., Giacobbo N., Bouffanais Y., Artale M. C., 2021, MNRAS, 502, 4877
Santoliquido F., Mapelli M., Artale M. C., Boco L., 2022, MNRAS, 516, 3297
Sarin N., Brandenburg A., Haskell B., 2023, ApJ, 952, L21
Schaye J. et al., 2014, MNRAS, 446, 521
Sengar R. et al., 2022, MNRAS, 512, 5782
Sgalletta C. et al., 2023, SEVN Parameter File from the Paper 'Binary Neutron Star Populations in the Milky Way', Zenodo, available at:https://doi.org/10.5281/zenodo.7887279
Shao Y., Li X.-D., 2018, ApJ, 867, 124
Smartt S. J. et al., 2017, Nature, 551, 75
Spera M., Mapelli M., 2017, MNRAS, 470, 4739
Spera M., Mapelli M., Giacobbo N., Trani A. A., Bressan A., Costa G., 2019, MNRAS, 485, 889
Spera M., Trani A. A., Mencagli M., 2022, Galaxies, 10, 76
Springel V., 2005, MNRAS, 364, 1105
Springel V., 2010, MNRAS, 401, 791
Stairs I. H., Thorsett S. E., Taylor J. H., Wolszczan A., 2002, ApJ, 581, 501
Stappers B. W., Keane E. F., Kramer M., Possenti A., Stairs I. H., 2018, Phil. Trans. R. Soc. London Ser. A, 376, 20170293
Stevenson S., Willcox R., Vigna-Gómez A., Broekgaarden F., 2022, MNRAS, 513, 6105
Szary A., Zhang B., Melikidze G. I., Gil J., Xu R.-X., 2014, ApJ, 784, 59
Tanvir N. R., Levan A. J., Fruchter A. S., Hjorth J., Hounsell R. A., Wiersema K., Tunnicliffe R. L., 2013, Nature, 500, 547
Tauris T. M., Manchester R. N., 1998, MNRAS, 298, 625
Tauris T. M., Langer N., Podsiadlowski P., 2015, MNRAS, 451, 2123
Tauris T. M. et al., 2017, ApJ, 846, 170
The EAGLE team, 2017, preprint (arXiv:1706.09899)
Thrane E., Osłowski S., Lasky P. D., 2020, MNRAS, 493, 5408
Tout C. A., Aarseth S. J., Pols O. R., Eggleton P. P., 1997, MNRAS, 291, 732
Troja E. et al., 2017, Nature, 551, 71
Tutukov A. V., Yungel'Son L. R., 1993, Astron. Rep., 37, 411
Urpin V., Konenkov D., 1997, MNRAS, 292, 167
Vigna-Gómez A. et al., 2018, MNRAS, 481, 4009
Vigna-Gómez A. et al., 2020, PASA, 37, e038
Virtanen P. et al., 2020, Nat. Methods, 17, 261
Webbink R. F., 1985, in Pringle J. E., Wade R. A., eds, Interacting Binary Stars. Cambridge Univ. Press, Cambridge, p. 39
Weisberg J. M., Huang Y., 2016, ApJ, 829, 55

Willcox R., Mandel I., Thrane E., Deller A., Stevenson S., Vigna-Gómez A., 2021, ApJ, 920, L37

Woosley S. E., 1987, in Helfand D. J., Huang J. H., eds, Proc. IAU Symp. Vol. 125, The Origin and Evolution of Neutron Stars. Kluwer, Dordrecht, p. 255

Yusifov I., Küçük I., 2004, A&A, 422, 545

Zhang C. M., Kojima Y., 2006, MNRAS, 366, 137

Zhang B. B. et al., 2022, preprint (arXiv:2205.07670)

APPENDIX A: KICK PRESCRIPTIONS

Fig. A1 shows the BNS merger rate in the MW for different natal kick models. Our Fiducial model, equivalent to the KGM20 model in Iorio et al. (2023), is described in Section 2.1. In models Kσ265 and Kσ150, we draw the kick magnitude from a Maxwellian distribution with one-dimensional root-mean square $\sigma = 265$ (Hobbs et al. 2005) and 150 km s^{-1} (Atri et al. 2019), respectively. These last two models are equivalent to Kσ265 and Kσ150 in Iorio et al. (2023). Fig. A1 shows that the natal kick model has a dramatic impact on the merger rate. In particular, our fiducial model is the only one that matches the observed rate, because it accounts for low natal kicks for stripped and ultra-stripped SNe (Giacobbo & Mapelli 2020). We will focus on the impact of natal kicks on the main properties of Galactic BNSs and black hole–NS systems in a follow-up study (Sgalletta et al. in preparation).
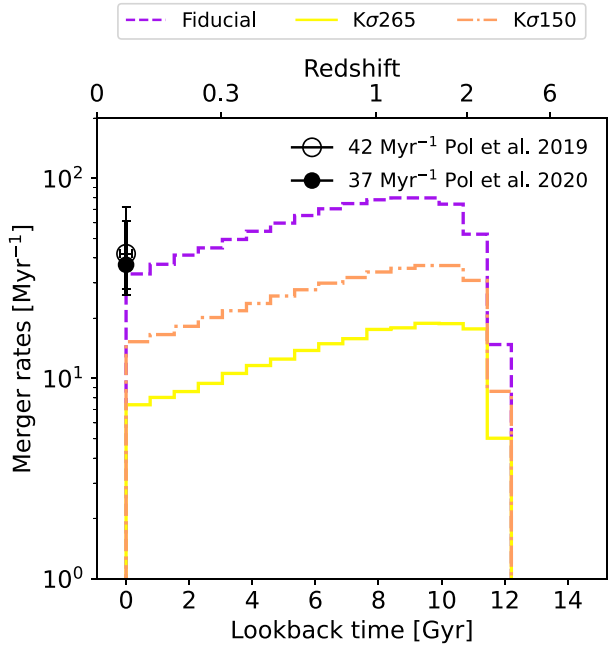
Figure A1. BNS merger rate in the MW as a function of the look-back time for different natal kick models. Purple dashed line: Fiducial model (Ua3t1Emp); pink dot–dashed line: Kσ265 model, yellow solid line: Kσ150 model. The circles show the BNS merger rate in the MW inferred from observations, as in Fig. 1. All simulations shown in this figure assume our fiducial model parameters: $\tau_{\rm d} = 1$Gyr, the U distribution for initial spins and magnetic fields, the Emp MW model and $\alpha = 3$. The natal kick model has a dramatic impact on the MW merger rate. Our fiducial model is the only one that matches the observed rate.

APPENDIX B: MASSES

Fig. B1 shows the BNS masses we obtained for the three core-collapse SN models we assumed (Section 2.1). The distributions computed with the rapid and delayed models by Fryer et al. (2012) produce a strong peak of the secondary mass at about 1.2 M$_\odot$, failing to reproduce the observed masses of the Galactic BNSs. In contrast, the rapid-gauss model matches the observed population by construction. We decided to exclude the masses from the statistical analysis in Section 3.5 because the only models that matches the observation does it by construction.
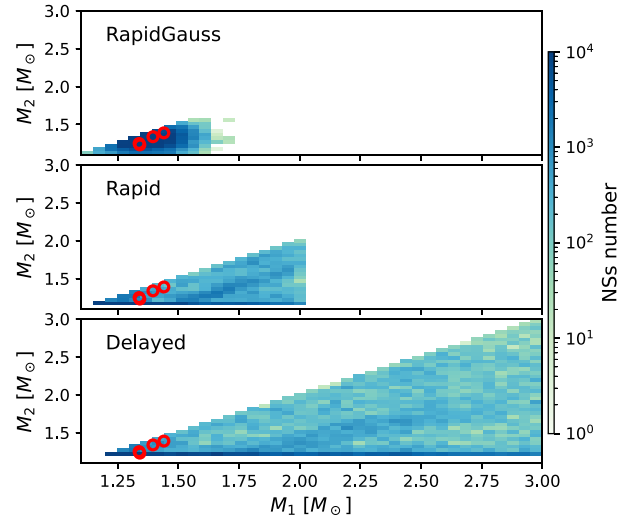
Figure B1. Secondary versus primary mass of the simulated BNSs, for the three different SN prescriptions adopted in this work. From top to bottom: Rapid-gauss, rapid, and delayed. Here, the primary (secondary) is the most (least) massive NS of each BNS. The colour shows the number of binaries in each cell. The red circles are the observed Galactic BNS masses (some of the circles overlap in this figure).

APPENDIX C: SKA SURVEY PARAMETERS

Table C1 shows the SKA survey parameters in the mid- and low-frequency ranges (Stappers et al. 2018) we used to obtain Table 7.

Table C1. Adopted parameters for the low- and mid-SKA surveys (Stappers et al. 2018). The columns show the bandwidth $\Delta\nu$, the antenna gain G_A, the system temperature $T_{\rm rec}$, the sampling time $\tau_{\rm sampl}$, the integration time $t_{\rm int}$ and the sky coverages, respectively.

Survey	$\Delta\nu$ (MHz)	G_A (K Jy^{-1})	$T_{\rm rec}$ (K)	$\tau_{\rm sampl}$ (ms)	$t_{\rm int}$ (s)	Sky Coverage
LOW	100	26.85	56	0.1	600	$-90° < \delta < 30°$
MID	300	3.92	20	0.1	600	$-90° < \delta < 30°$

This paper has been typeset from a TeX/LaTeX file prepared by the author.